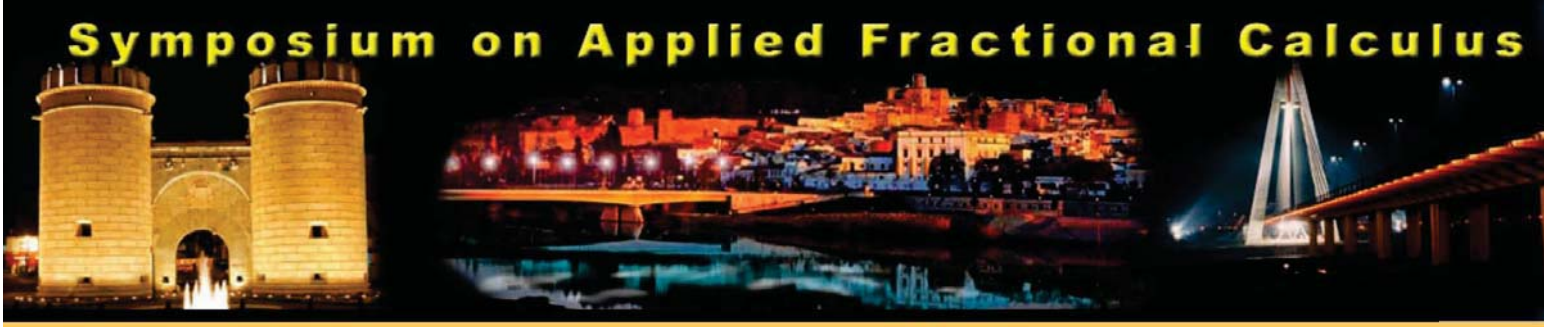

Symposium on Applied Fractional Calculus

Badajoz (Industrial Engineering School), October 15-17, 2007

JUNTA DE EXTREMADURA

JUNTA DE EXTREMADURA
Consejería de Infraestructuras y Desarrollo Tecnológico

UEX

ESCUELA DE INGENIERIAS INDUSTRIALES

Real Sociedad Española de Física

R.S.E.F.

consolider ingenio i-math mathematica ingenio2010

TOWARDS THE APPLICATION OF FRACTIONAL CALCULUS IN ENGINEERING SCIENCES

J. A. Tenreiro Machado[*], Ramiro S. Barbosa [*], Isabel S. Jesus[*], Manuel F. Silva[*]
Cecília Reis[*], Luís M. Afonso[*], Maria G. Marcos[*], Miguel F. M. Lima[#], Eduardo S. Pires[+]

[*]Institute of Engineering of Porto
Porto, Portugal, {jtm,rsb,isj,mss,cmr,lma,mgm}@isep.ipp.pt
[#]School of Technology of Viseu
Viseu, Portugal, lima@mail.estv.ipv.pt
[+]University of Trás-os-Montes and Alto Douro
Vila Real, Portugal, epires@marao.utad.pt

Abstract: This article illustrates several applications of Fractional Calculus (FC) in engineering sciences. This mathematical tool will be used here to model, analyze and control various dynamical systems, such as the Van der Pol oscillator, legged robots, electrical systems, digital circuit synthesis, evolutionary computing, redundant robots and financial modelling. Their effectiveness and utility will be demonstrated.

Keywords: Fractional calculus, control, modelling, dynamics.

1. INTRODUCTION

In recent years Fractional Calculus (FC) has been a fruitful field of research in science and engineering (Hilfer, 2000; Miller and Ross, 1993; Oldham and Spanier, 1974; Oustaloup, 1991, 1995; Podlubny, 1999; Samko *et al.*, 1993). In fact, many scientific areas are currently paying attention to the FC concepts and we can refer its adoption in viscoelasticity and damping, diffusion and wave propagation, electromagnetism, chaos and fractals, heat transfer, biology, electronics, signal processing, robotics, system identification, traffic systems, genetic algorithms, percolation, modelling and identification, telecommunications, chemistry, irreversibility, physics, control systems, economy and finance.

The FC deals with derivatives and integrals to an arbitrary order (real or, even, complex order). The mathematical definition of a derivative/integral of fractional order has been the subject of several different approaches (Miller and Ross, 1993; Oldham and Spanier, 1974; Podlubny, 1999; Samko *et al.*, 1993). For example, the Laplace definition (L) of a fractional derivative/integral of a signal $x(t)$ is given through the following expression:

$$L\left\{D^{\alpha} x(t)\right\} = s^{\alpha} X(s) - \sum_{k=0}^{n-1} s^{k} D^{\alpha-k-1} x(t)\Big|_{t=0} \qquad (1)$$

where $X(s) = L\{x(t)\}$. Considering null initial conditions, Eq. (1) reduces to the simple form ($\alpha \in \Re$):

$$L\left\{x(t)\right\} = s^{\alpha} X(s) \qquad (2)$$

which is a direct generalization of the integer-order scheme with the multiplication of the signal transform $X(s)$ by the Laplace s-variable raised to a fractional value α.

Another useful definition, commonly used into numerical schemes, is the Grünwald-Letnikov definition, given by ($\alpha \in \Re$):

$$D^{\alpha} x(t) = \lim_{h \to 0}\left[\frac{1}{h^{\alpha}} \sum_{k=0}^{\infty} (-1)^{k} \binom{\alpha}{k} x(t-kh)\right] \qquad (3a)$$

$$\binom{\alpha}{k} = \frac{\Gamma(\alpha+1)}{\Gamma(k+1)\Gamma(\alpha-k+1)} \qquad (3b)$$

where Γ is the Gamma function and h is the time increment. Expression (3) shows that fractional-order operators are "global" operators having a memory of

all past events, making them adequate for modelling memory and hereditary effects in most materials and systems.

The Riemann-Liouville definition is used from a continuous point of view and has the form ($n-1<\alpha<n$, $\alpha>0$):

$$D^{\alpha}x(t)=\frac{1}{\Gamma(n-\alpha)}\frac{d^n}{dt^n}\int_0^t\frac{x(\tau)}{(t-\tau)^{\alpha-n+1}}d\tau \qquad (4)$$

Bearing these ideas in mind, sections 2-10 present several applications of FC in engineering sciences. In section 11 we draw the main conclusions.

2. VAN DER POL OSCILLATOR OF FRACTIONAL ORDER

The study of nonlinear oscillators has been important in the development of the theory of dynamical systems. The Van der Pol oscillator (VPO), described by a second-order nonlinear differential equation, can be regarded as describing a mass-spring-damper system with a nonlinear position-dependent damping coefficient or, equivalently, an RLC electrical circuit with a negative-nonlinear resistor, and has been used for developing models in many applications, such as electronics, biology or acoustics.

In the standard form, it is given by a second-order nonlinear differential equation of type:

$$\ddot{x}+\alpha(x^2-1)\dot{x}+x=0 \qquad (5)$$

or, in state-space form, as:

$$\begin{bmatrix}\dot{x}_1\\ \dot{x}_2\end{bmatrix}=\begin{bmatrix}0 & 1\\ -1 & -\alpha(x_1^2-1)\end{bmatrix}\begin{bmatrix}x_1\\ x_2\end{bmatrix} \qquad (6)$$

where $\alpha>0$ is the control parameter that reflects the degree of nonlinearity of the system. Eq. (5) possesses a periodic solution that attracts other solution except the trivial one at the unique equilibrium point $x=\dot{x}=0$.

A fractional version is now considered by introducing a fractional time derivative of order λ in state space equations (6) of the standard VPO, yielding (Barbosa *et al.*, 2004b):

$$\begin{bmatrix}x_1^{(\lambda)}\\ \dot{x}_2\end{bmatrix}=\begin{bmatrix}0 & 1\\ -1 & -\alpha(x_1^2-1)\end{bmatrix}\begin{bmatrix}x_1\\ x_2\end{bmatrix} \qquad (7)$$

which corresponds to the differential equation:

$$x^{(1+\lambda)}+\alpha(x^2-1)x^{(\lambda)}+x=0,\quad 0<\lambda<1 \qquad (8)$$

Note that system (8) reduces to the classical VPO (4) when $\lambda=1$ and that the total system order is changed to $\lambda+1<2$.

Figure 1 illustrates the block diagram representation of system (8). As can be seen, the fractional VPO system is implemented by using a fractional integrator $1/s^{\lambda}$ of order $0<\lambda<1$. The fractional-order integrator is an irrational transfer function in the Laplace s-variable. This type of systems has an unlimited memory which precludes its direct utilization in time-domain simulations. Therefore, the usual approach is the development of integer-order approximations that approximate (up to a given degree of accuracy) the fractional-order operators. So, in order to effectively analyze the fractional-order system of Fig. 1, we develop rational approximations for the fractional-order integrator $1/s^{\lambda}$. In this perspective, we adopt the approximation frequency method described by Charef *et al*. (1992), known as "Singularity Function Method". These approximations were obtained for $\lambda\in\,]0,\ 1[$, frequency range of $\omega=[0.01,\ 100]$ rad/s and a maximum discrepancy from the ideal response of $\Delta=2$ dB.

Figure 2 shows the phase portraits for initial conditions $x_1(0)=0$ and $x_2(0)=1$ as the fractional-order λ (Fig. 2a)) and the control parameter α (Fig. 2b) are varied, respectively. In both cases, we verify significant variations of the limit cycle, revealing a large impact of the λ-order derivative upon system dynamics. In order to clarify this point, Fig. 3 illustrates the amplitude A and the period T of the output oscillation. It is clearly seen the large variation of the limit cycle, particularly in the period of the oscillation.

Figure 4 shows the steady-state time responses and the Fourier spectra of the output $x_1(t)$ for several values of λ and for $\alpha=5$. The frequency spectrum was evaluated by using the FFT over $N=2^{15}$ points after elapsing the initial transient of the signal output $x_1(t)$. Once more, we observe the variation of the limit cycle as function of λ, noting that the amplitude gets smaller as λ is decreased. On the other hand, analysing the Fourier spectra, we verify that the multiplicity of peaks and the amplitude of these peaks varies with α, which is in accordance with the time responses. Also note that the energy of the output signal, is not only concentrated in the peaks (fundamental and integer-odd harmonics), but distributed along all frequency domain, showing a long-term behaviour indicating different amplitude decays depending on λ (Barbosa *et al.*, 2004b).

The results reveal that the fractional version of the VPO system can exhibit different behaviour from those obtained with the standard Van der Pol oscillator depending on order's derivative (or system's order). The fractional-order can act as a modulation parameter that may be useful for a better understanding and control of such systems.

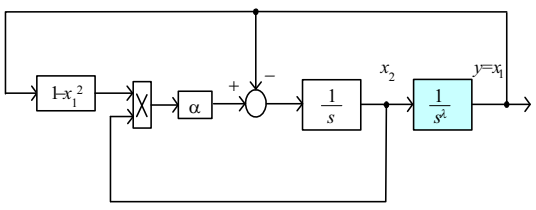

Fig. 1. Block diagram of the fractional Van der Pol system.

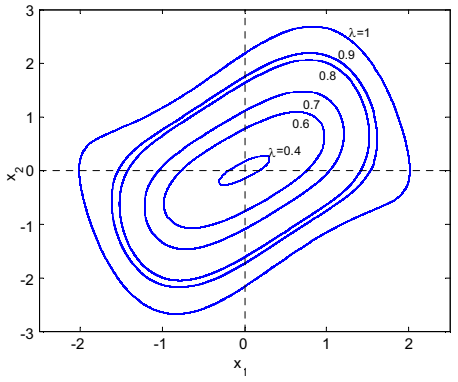

a)

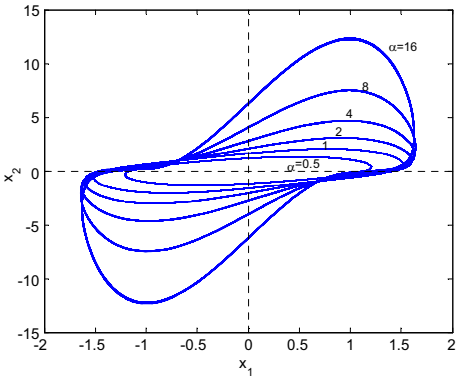

b)

Fig. 2. Phase portraits: a) $\lambda = \{0.4, 0.6, 0.7, 0.8, 0.9, 1.0\}$ and $\alpha = 1$, b) $\lambda = 0.8$ and $\alpha = \{0.5, 1, 2, 4, 8, 16\}$.

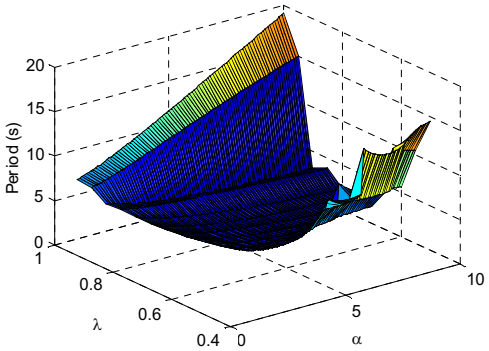

a)

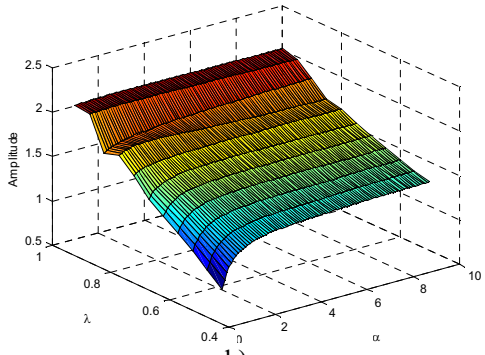

b)

Fig. 3. Limit cycle: a) period and b) amplitude of the output oscillation for $1 \leq \alpha \leq 10$ and $0.5 \leq \lambda \leq 1$.

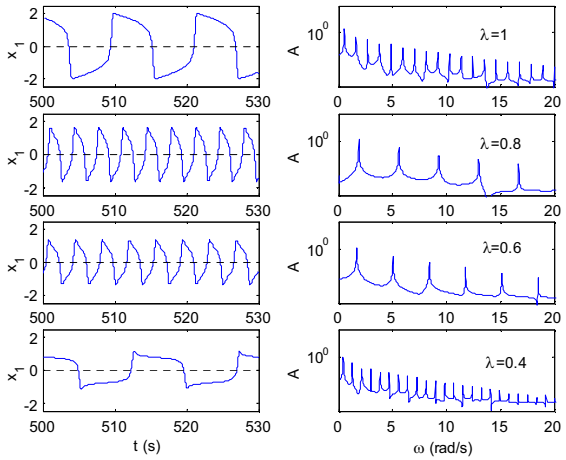

Fig. 4. Time responses and Fourier spectra for $\lambda = \{1, 0.8, 0.6, 0.4\}$ and $\alpha = 5$.

3. FRACTIONAL ORDER COMPLEX DYNAMICS AND CONTROL OF LEGGED ROBOTS

Walking machines allow locomotion in terrain inaccessible to other type of vehicles, since they do not need a continuous support surface, but at the cost of higher requirements for leg coordination and control. For these robots, joint level control is usually implemented through a PID like scheme. The application of the theory of fractional calculus in robotics joint control is still in a research stage, but the recent progress in this area reveals promising aspects for future developments (Silva *et al.*, 2003a).

In this line of thought, the first part of this study evaluates foot-ground interaction during the robot locomotion, for several walking conditions, and analyzes its dynamics in the viewpoint of fractional calculus. The main interest of this study stems from previous works showing that fractional dynamics arise in systems with "mixed" characteristics, such as the cases of a liquid interaction with a porous wall, in biological systems where there is the growth of tumors in healthy tissues and in backlash systems with continuous-discrete interactions (Silva *et al.*, 2006a).

The system under analysis reveals a behavior of this kind, namely with multiple periodic collisions among the robot feet and the ground. For example, at the beginning of the support phase of each foot, although not desirable, often the contact of the foot with the ground is established and lost several times before stabilizing.

We consider a hexapod walking system (Fig. 5) with $n = 6$ legs, equally distributed along both sides of the robot body, having each two rotational joints (*i.e.*, $j = \{1, 2\} \equiv \{\text{hip, knee}\}$) (Silva *et al.*, 2005).

Figure 5 presents the dynamic model for the hexapod body and foot-ground interaction. It is considered robot body compliance because walking animals have a spine that allows supporting the locomotion

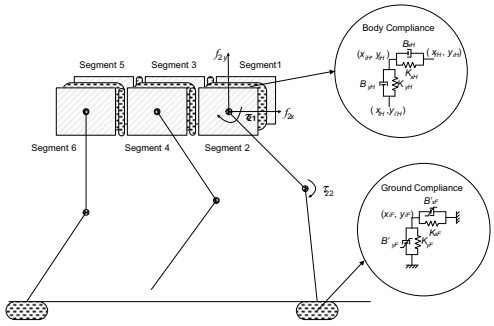

Fig. 5. Model of the robot body and foot-ground interaction.

with improved stability. The robot body is divided in n identical segments (each with mass $M_b n^{-1}$) and a linear spring-damper system (with parameters defined so that the body behaviour is similar to the one expected to occur on an animal) is adopted to implement the intra-body compliance (Silva *et al.*, 2005). The contact of the ith robot feet with the ground is modelled through a non-linear system (Silva *et al.*, 2003b), being the values for the parameters based on the studies of soil mechanics (Silva *et al.*, 2003b).

In order to obtain the transfer functions (TF) of the system (i.e., the robot and the environment), the frequency response of the locomotion system is computed numerically. For that purpose, small amplitude sinusoidal exciting signals $\boldsymbol{\delta p_d}(t)$ are superimposed, separately, on the frequency range under analysis, over the x and y feet desired Cartesian trajectories, according to the block diagram presented in Fig. 6.

The resulting feet reference trajectories are given by:

$$\mathbf{p_d}(t)+\boldsymbol{\delta p}(t)=\begin{bmatrix} x_{id}(t)+\delta x_{id}(t) \\ y_{id}(t)+\delta y_{id}(t) \end{bmatrix} \tag{9a}$$

$$\mathbf{p_d}(t)+\boldsymbol{\delta p}(t)=\boldsymbol{\psi}\left[\boldsymbol{\theta_d}(t)+\boldsymbol{\delta\theta_d}(t)\right] \Rightarrow$$
$$\Rightarrow \boldsymbol{\theta_d}(t)+\boldsymbol{\delta\theta_d}(t)=\boldsymbol{\psi}^{-1}\left[\mathbf{p_d}(t)+\boldsymbol{\delta p}(t)\right] \tag{9b}$$

where $\mathbf{p_d}(t)$ + $\boldsymbol{\delta p_d}(t)$ are the ith feet desired Cartesian trajectories (relatively to their hip) perturbed with a sinusoidal signal of small amplitude and $\boldsymbol{\Theta_d}(t)$ + $\boldsymbol{\delta\Theta_d}(t)$, are the corresponding perturbed joint trajectories. During the robot locomotion simulation, the perturbations propagate to the torques demanded to the robot leg joint actuators by the controller (resulting $\boldsymbol{\Gamma_C}(t)$ + $\boldsymbol{\delta\Gamma_C}(t)$) and to the robot real feet trajectories (that become $\mathbf{p_F}(t)$ + $\boldsymbol{\delta p}(t)$).

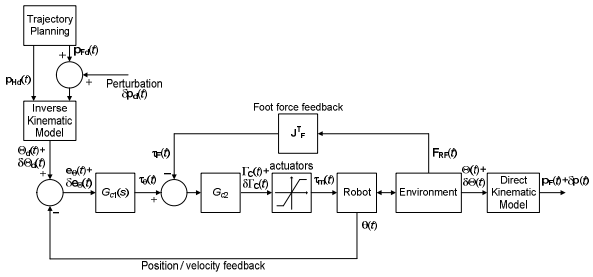

Fig. 6. Block diagram adopted for the calculation of the transfer functions $G_{xj}(s)$ and $G_{yj}(s)$, j = 1,2.

The system TFs are given by (j = 1, 2):

$$G_{xj}(s)=\frac{F\left\{\delta x_{1F}(t)\right\}}{F\left\{\delta\tau_{1jC}(t)\right\}} \tag{10a}$$

$$G_{yj}(s)=\frac{F\left\{\delta y_{1F}(t)\right\}}{F\left\{\delta\tau_{1jC}(t)\right\}} \tag{10b}$$

where $\delta x_{1F}(t)$ and $\delta y_{1F}(t)$ are the resulting leg 1 foot trajectory perturbations, $\tau_{11C}(t)$ and $\tau_{12C}(t)$ are the corresponding joint demanded torques perturbations and $F\{\}$ represents the Fourier Transform operator.

In a first phase we develop a set of simulations to analyze the TFs of the hexapod-environment system for two different velocities, namely V_F = 1.0 ms^{-1} and V_F = 2.0 ms^{-1}.

In order to determine G_{xj} and G_{yj} (j = 1,2), the locomotion is simulated while the robot is moving on a perfectly flat surface without obstacles in its path. For this purpose, sinusoidal perturbations, with maximum amplitudes of $\delta x_{id}(t)$ = 10^{-4} m and $\delta y_{id}(t)$ = 10^{-4} m in the x and y directions, respectively, are superimposed, separately, over the planned robot feet Cartesian trajectories, in the range of frequencies 0.001 rads^{-1} ≤ ω ≤ 100.0 rads^{-1} during $Tsim$ ≈ 40000 steps (Silva *et al.*, 2006a).

We start with G_{xj} for a robot forward locomotion speed of V_F = 1.0 ms^{-1}. As can be observed from the Nichols chart presented in Fig. 7, G_{x1} presents different asymptotes for different frequency ranges.

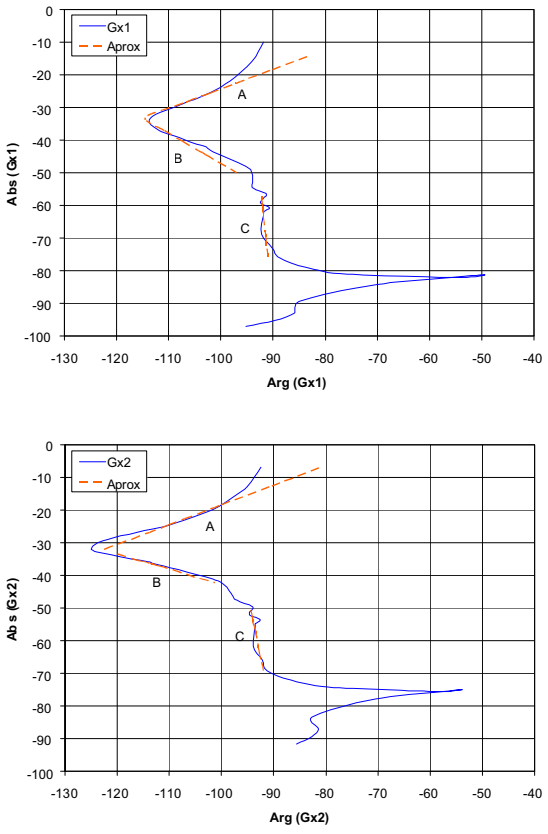

Fig. 7. Nichols charts of $G_{x1}(j\omega)$ and $G_{x2}(j\omega)$, and their approximations at low (A), medium (B) and high frequencies (C), for V_F = 1.0 ms^{-1}.

At low frequencies (A ≡ [0.001; 0.05] rads^{-1}) the asymptote can be approximated by the expression:

$$G_{xj}(s) \approx \frac{k_{xj}}{j\left(s^{\alpha_{xj}+j\beta_{xj}}\right)}, j=\sqrt{-1}, \alpha_{xj}, \beta_{xj} \in \Re, j=1,2 \quad (11)$$

The values of the parameters K_{xj}, α_{xj} and β_{xj} for the low frequency asymptotic approximation of G_{x1} are presented in Table 1.

At medium and at high frequencies (regions B ≡ [0.05; 0.5] rads^{-1} and C ≡ [0.5; 5.0] rads^{-1}), the resulting TFs can be approximated by an expression of the type:

$$G_{xj}(s) \approx \frac{k_{xj}}{s^{\alpha_{xj}+j\beta_{xj}}}, \alpha_{xj}, \beta_{xj} \in \Re, j=1,2 \quad (12)$$

The values of the parameters K_{xj}, α_{xj} and β_{xj} for the asymptotic approximations in these frequency ranges are also presented in Table 1.

These results reveal a complex order dynamics that is a consequence of the foot-ground interaction, with several free-impact-contact-impact-free dynamical states.

We verify that the Nichols chart of G_{x2} has similar features to those of G_{x1}, as can be observed in Fig. 7. The asymptotic approximations at low, medium and high frequencies, can be described by identical expressions and occur in the same frequency ranges as for the case of G_{x1}. The same can be concluded by comparing the values of the parameters α_{xj} and β_{xj}, for the asymptotic approximations of G_{x2} and G_{x1} (Table 1).

This study is repeated for a robot velocity of $V_F = 2.0$ ms^{-1} and the conclusions are identical.

The meaning of the imaginary factor j in the denominator of expression (11) in not yet clear. However, the authors believe on the existence of an expression unifying the asymptotic behavior of the TF both at low and medium frequencies, which is currently under investigation. One possibility, under study, is to replace the $s^{\alpha+j\beta}$, that leads to complex-valued outputs, by one of the operators $H_1(s) = s^{\alpha+j\beta} + s^{\alpha-j\beta}$ or $H_2(s) = j[s^{\alpha+j\beta} - s^{\alpha-j\beta}]$ that lead to real valued outputs. Supporting this consideration we have the similarities between the values of the parameters α_{xj} and β_{xj} (i.e., complex conjugate exponents for regions A and B) for the low and medium frequency asymptotic approximations of G_{xj} (j = 1, 2).

Table 1 - Parameters values for the asymptotic approximations of the Nichols charts of G_{x1} and G_{x2}, with V_F =1.0 ms^{-1}

V_F =1.0 ms^{-1}	G_{x1}			G_{x2}		
Frequency Range	k_{x1}	α_{x1}	β_{x1}	k_{x2}	α_{x2}	β_{x2}
Low (A)	0.001	0.72	0.18	0.001	0.77	0.22
Medium (B)	0.0014	0.84	-0.20	0.0022	1.03	-0.19
High (C)	0.00068	1.02	-0.01	0.002	1.04	-0.04

Based on the previous results, the second part of this study compares two different robot controllers, namely Proportional and Derivative (*PD*) and Fractional Order (*FO*) algorithms, in the presence of joints with viscous friction, flexibility and backlash.

In a first phase, we consider that the joint actuators and transmissions are ideal, as presented in Fig. 8a. Afterwards, in a second phase, we consider that the joint transmissions are non ideal, exhibiting a compliant behaviour (Fig. 8b). Finally, in a third phase we consider that the joint transmissions also include backlash (Fig. 8c), which causes the occurrence of impacts at the gear. These collisions obey the principle of conservation of Momentum, and the Newton's law.

The general control architecture of the hexapod robot is presented in Fig. 9 (Silva *et al*., 2006b). In this study we evaluate the effect of different PD$^{\alpha}$, $\alpha \in \Re$, controller implementations for $G_{c1}(s)$, while G_{c2} is a proportional controller with gain $Kp_j = 0.9$ (j = 1, 2). For the PD$^{\alpha}$ algorithm, implemented through a discrete-time 4th-order Padé approximation (a_{ij}, $b_{ij} \in \Re$, j = 1, 2), we have:

$$G_{c1\,j}(z) \approx Kp_j + K\alpha_j \sum_{i=0}^{i=u} a_{ij}\, z^{-i} \Big/ \sum_{i=0}^{i=u} b_{ij}\, z^{-i} \quad (13)$$

where Kp_j and $K\alpha_j$ are the proportional and derivative gains, respectively, and α_j is the fractional order, for joint j. Therefore, the classical PD^1 algorithm occurs when the fractional order $\alpha_j = 1.0$.

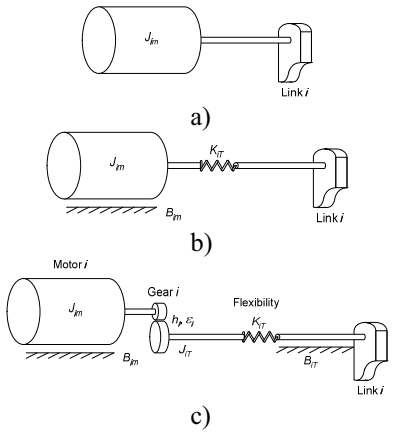

Fig. 8. Model of the leg joint: a) ideal actuator and transmission, b) actuator with friction and transmission flexibility, and c) actuator and transmission with friction, flexibility and backlash.

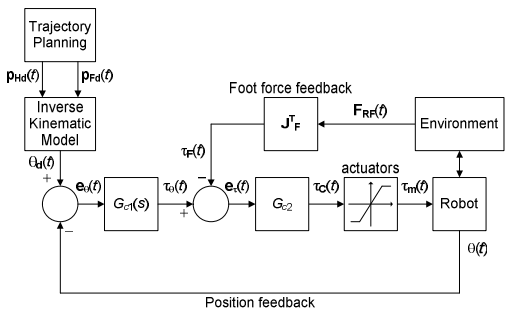

Fig. 9. Hexapod robot control architecture.

The analysis is based on the formulation of two indices measuring the mean absolute density of energy per traveled distance (E_{av}) and the hip trajectory errors (ε_{xyH}) during walking, according to:

$$E_{av} = \frac{1}{d}\sum_{i=1}^{n}\sum_{j=1}^{m}\int_0^T \left|\boldsymbol{\tau}_{ij}(t)\dot{\boldsymbol{\theta}}_{ij}(t)\right| dt \quad \left[\mathrm{Jm}^{-1}\right] \qquad (14a)$$

$$\varepsilon_{xyH} = \sum_{i=1}^{n}\sqrt{\frac{1}{N_s}\sum_{k=1}^{N_s}\left(\Delta_{ixH}{}^2 + \Delta_{iyH}{}^2\right)} \quad [\mathrm{m}]$$
$$\Delta_{ixH} = x_{iHd}(k) - x_{iH}(k),\ \Delta_{iyH} = y_{iHd}(k) - y_{iH}(k) \qquad (14b)$$

To tune the controller we adopt a systematic method, testing and evaluating several possible combinations of parameters, for all controller implementations. Therefore, we adopt the $G_{c1}(s)$ parameters that establish a compromise in what concerns the simultaneous minimisation of E_{av} and ε_{xyH}. Moreover, it is assumed high performance joint actuators, with a maximum actuator torque of $\tau_{ijMax} = 400$ Nm.

In order to make a proper comparison of both controllers, we establish a compromise in what concerns the minimisation of ε_{xyH} and E_{av}, on which the *PD* and the *FO* controllers present similar values for the indices ε_{xyH} and E_{av} and the motor torques and hip errors are also almost identical.

With these controller settings, we analyse the system performance for the three different dynamical effects on the leg joints. Therefore, we start by considering an ideal joint transmission and, afterwards, we augment the model by including viscous friction, flexibility and backlash. The performance of both controllers is evaluated for the three cases, from the viewpoint of the proposed indices, while considering different levels of actuator saturation. We consider the *PD* controller and different values of τ_{ijMax}, in order to observe its influence upon the performance indices and, in a second phase, we repeat the experiments for the case of a *FO* controller.

For the ideal transmission, the index E_{av} presents no significant variation for moderate saturation levels (*e.g.*, $\tau_{ijMax} > 120$ Nm) being the performance of both controllers approximately similar. In the case of strong actuator saturation (*e.g.*, $\tau_{ijMax} < 100$ Nm) the index reveals a large degradation with difficulties both for the *PD* and the *FO* algorithms. Nevertheless, this situation is not realistic since it corresponds to operating conditions requiring joint torques much higher than those established by the saturation level. On the other hand, as expected, the robot hips trajectories errors are higher the smaller the maximum actuator torque. When comparing this index, for both control algorithms, we conclude that the *PD* controller presents smaller values of the index ε_{xyH}, for the entire range of variation of τ_{ijMax}.

The second situation consists of actuator model with viscous friction and joint transmission with flexibility. For this case the *FO* controller presents the lower values for the two indices (along most of the range of variation of K_{ijT} that keeps the robot locomotion stable) being the effect more noticeable the smaller the values of τ_{ijMax}.

On a third set of experiments we consider that the joint transmission model includes viscous friction, flexibility and backlash. For this case, the *FO* controller presents also lower values for the performance indices $\{E_{av}, \varepsilon_{xyH}\}$ than the *PD* controller. This effect is more pronounced for smaller values of τ_{ijMax} and is visible on a large range of variation of the flexibility K_{ijT}, that keep the robot locomotion stable.

The same conclusion is valid for the entire range of variation of the restitution coefficient ε_{ij} and on a large range of variation of the backlash width h_{ij} (Figs. 10 – 11).

From the above experiments we can conclude that the *FO* controller presents superior results when we have actuator saturation and dynamical phenomena on the joints. This means that, although tuned for identical performance in an ideal situation, the *FO* algorithm is more robust in a real operating condition.

4. ELECTRICAL IMPEDANCE OF FRUITS

In an electrical circuit the voltage $u(t)$ and the current $i(t)$ can be expressed as a function of time t:

$$u(t) = U_0\cos(\omega t) \qquad (15)$$

$$i(t) = I_0\cos(\omega t+\phi) \qquad (16)$$

where U_0 and I_0 are the amplitudes of the signals, ω is the frequency and ϕ is the current phase shift. The voltage and current can be expressed in complex form as:

$$u(t) = \mathrm{Re}\left\{U_0 e^{j(\omega t)}\right\} \qquad (17)$$

$$i(t) = \mathrm{Re}\left\{I_0 e^{j(\omega t+\phi)}\right\} \qquad (18)$$

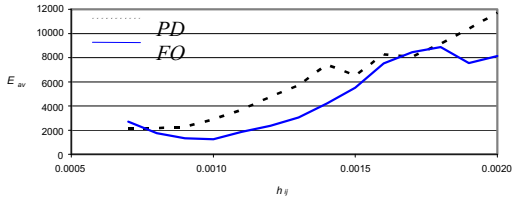

Fig. 10. Plot of E_{av} *vs*. h_{ij} for the *PD* and *FO* controllers, with $\tau_{ijMax} = 100$ Nm.

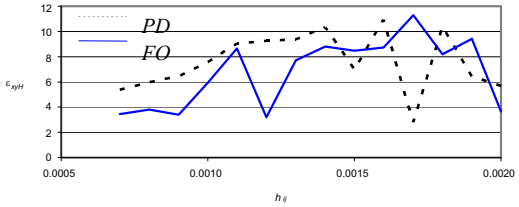

Fig. 11. Plot of ε_{xyH} *vs.* h_{ij} for the *PD* and *FO* controllers, with $\tau_{ijMax} = 100$ Nm.

Consequently, the electrical impedance $Z(j\omega)$ is:

$$Z(j\omega) = \frac{U(j\omega)}{I(j\omega)} = Z_0 e^{j\phi} \quad (19)$$

A brief reference about the constant phase elements (CPE) and Warburg impedance is presented here due to their application in the work. In fact, to model an electrochemical phenomenon it is often used a CPE because the surface is not homogeneous (Barsoukov and Macdonald, 2005; Jesus *et al.*, 2006a). So, with a CPE:

$$Z(j\omega) = \frac{1}{(j\omega)^{\alpha} C} \quad (20)$$

C is the capacitance, with units $[m^{-2/\alpha}\, kg^{-1/\alpha}\, s^{(\alpha+3)/\alpha}\, A^{2/\alpha}]$, and α is a parameter that can change between 0 and 1, being an ideal capacitor for $\alpha = 1$.

On the other hand, in electrochemical systems with diffusion, the impedance is modeled by the so-called Warburg element (Jesus *et al.*, 2006a; Jonscher, 1993; Hirad *et al.*, 1998). The Warburg element arises from one-dimensional diffusion of an ionic species to the electrode. If the impedance is under an infinite diffusion layer, the Warburg impedance is:

$$Z(j\omega) = \frac{R}{(j\omega)^{0.5} C} \quad (21)$$

where R is the diffusion resistance. If the diffusion process has finite length, the Warburg element becomes:

$$Z(j\omega) = R \frac{\tanh(j\omega\tau)^{0.5}}{(\tau)^{0.5}} \quad (22)$$

with $\tau = \delta^2 / D$, where R is the diffusion resistance, τ is the diffusion time constant, δ is the diffusion layer thickness and D is the diffusion coefficient.

4.1 Study of Fractional Order Electrical Impedances

The structure of fruits and vegetables have cells that are sensitive to heat, pressure and other stimuli. These systems constitute electrical circuits exhibiting a complex behaviour.

Bearing these facts in mind, in our work we study the electrical impedance for several botanical elements, under the point of view of fractional order systems.

We apply sinusoidal excitation signals $v(t)$, to the botanical system, for several distinct frequencies ω (Fig. 12) and the impedance $Z(j\omega)$ is measured based on the resulting voltage $u(t)$ and current $i(t)$.

Moreover, we measure the environmental temperature, the weight, the length and width of all botanical elements. This criterion helps us to understand how these factors influence $Z(j\omega)$.

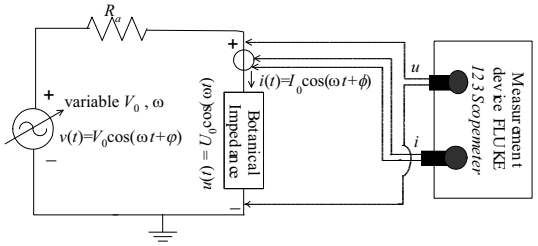

Fig. 12. Electrical circuit for the measurement of the botanical impedance $Z(j\omega)$.

In this study we develop several different experiments for evaluating the variation of the impedance $Z(j\omega)$ with the amplitude of the input signal V_0, for different electrode lengths of penetration inside the element Δ, the environmental temperature T, the weights W and the dimension D.

The value of R is changed for each experiment, in order to adapt the values of the voltage and current to the scale of the measurement device.

We start by analyzing the impedance for an amplitude of input signal of $V_0 = 10$ volt, a constant adaptation resistance R_a = 15 kΩ, applied to one *Solanum Tuberosum* (potato), with an weight $W = 1.24\ 10^{-1}$ kg, environmental temperature $T = 26.5$ degree Celsius, dimension $D = 7.97\ 10^{-2} \times 5.99\ 10^{-2}$ m, and the electrode length penetration $\Delta = 2.1\ 10^{-2}$ m.

Figure 13 presents the Bode diagrams for $Z(j\omega)$. The results reveal that the system has a fractional order impedance. In fact, approximating the experimental results in the amplitude Bode diagram through a power function namely by $|Z(j\omega)| = a\omega^{-b}$, we obtain $(a, b) = (4.91\ 10^3, 0.0598)$, at the low frequencies, and $(a, b) = (7.94\ 10^5, 0.5565)$, at the high frequencies.

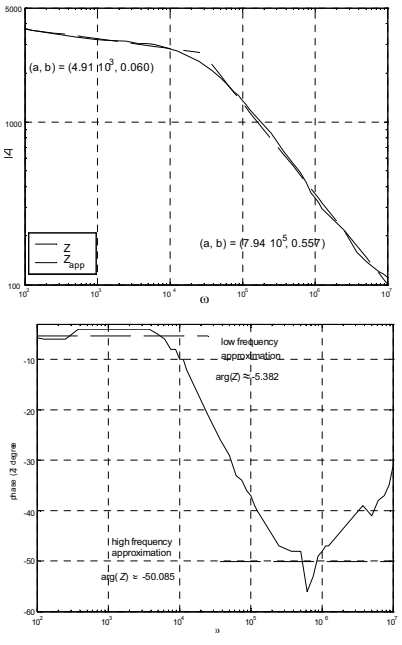

Fig. 13. Bode diagrams of the impedance $Z(j\omega)$ for the potato.

It is interesting to compare the polar diagram and the admittance loci for *RLC*, series or parallel, circuits. We verify that our systems have similarities with the *RC* parallel circuit and, therefore, we conclude that this vegetable has proprieties similar to a kind of capacitor. In order to analyze the system linearity we evaluate $Z(j\omega)$ for different amplitudes of input systems, namely, $V_0 = \{5, 15, 20\}$ volt, maintaining constant the adaptation resistance $R_a = 15$ kΩ.

The impedance $Z(j\omega)$ has a fractional order and this characteristic does not change significantly with the variation of input signal amplitude (Table 2). Therefore, we can conclude that this system has a linear characteristic.

In a second experiment, we vary the length Δ of the electrode penetration inside the potato, and we evaluate its influence upon the value of the impedance. Therefore, we adjust the electrode to $\Delta = 1.42\ 10^{-2}$ m, with $V_0 = 10$ volt and adaptation resistance $R_a = 5$ kΩ, leading to $|Z(j\omega)|$ approximations $(a, b) = (5.48\ 10^3, 0.0450)$, at the low frequencies, and $(a, b) = (1.00\ 10^6, 0.5651)$, at the high frequencies. With these results, we conclude that the length of wire inside the potato does not change significantly the values of the fractional orders. Also the linearity was again confirmed. The last experiment with the potato is related with the variation of environmental temperature. In this case, we use the first potato and the same conditions of first experience, but with an temperature $T = 25.7$ degree Celsius. The amplitude impedance $|Z(j\omega)|$ has the values: $(a, b) = (8.91\ 10^3, 0.0555)$, at the low frequencies, and $(a, b) = (7.10\ 10^5, 0.5010)$, at the high frequencies. Once more we verify the small variation of the fractional order.

Another issue that may influence the results is the weight. Therefore, we apply an input signal with amplitude $V_0 = 10$ volt, adaptation resistance $R_a = 15$ kΩ, with environmental temperature $T = 26.5$ degree Celsius, and electrode penetration $\Delta = 2.1\ 10^{-2}$ m to another potato with dimension $D = 7.16\ 10^{-2} \times 3.99\ 10^{-2}$ m, weight $W = 5.89\ 10^{-2}$ kg. The asymptotic results for $|Z(j\omega)|$ are $(a, b) = (7.17\ 10^3, 0.0546)$, at the low frequencies and $(a, b) = (2.00\ 10^6, 0.5990)$, at the high frequencies. Again, this experience does not reveal significant variations in the fractional order while the linearity is also confirmed.

In conclusion, the impedance does not change significantly with the factors analyzed. In this line of thought, we organize similar experiments with other vegetables and fruits.

Table 2. Comparison of the values of $|Z(j\omega)| \approx a\omega^{-b}$ for different amplitudes of the input signal

Amplitude	low ω		high ω	
(volt)	***a***	***b***	***a***	***b***
5	$4.79\ 10^3$	0.062	$6.52\ 10^5$	0.542
10	$4.91\ 10^3$	0.060	$7.94\ 10^5$	0.557
15	$4.54\ 10^3$	0.054	$5.66\ 10^5$	0.530
20	$4.65\ 10^3$	0.055	$5.86\ 10^5$	0.530

The results correspond to experiments adopting an amplitude of input signal $V_0 = 10$ volt and an electrode penetration $\Delta = 2.1\ 10^{-2}$ m. Similar experiments are developed for several fruits. Table 3 presents the characteristics of the vegetables and fruits respectively.

Figure 14 depicts Re $\{Z(j\omega)\}$ and Im $\{Z(j\omega)\}$ for some of the vegetables and fruits under study, and the corresponding approximation values. In these experiences, the adaptation resistance R_a is changed for each case.

The results reveal that $Z(j\omega)$ has distinct characteristics according with the frequency range. For low frequencies, the impedance is approximately constant, but for high frequencies, it is clearly of fractional order.

4.2 The Impedance Model

In the previous section we verified that it is difficult to find a model for $Z(j\omega)$ within the whole frequencies range. In this section, we apply the circuit of Fig. 15, often adopted in the area of electrochemistry, where R_0 and R_1 are resistances and *CPE* is given in (20).

The numerical values of R_0, R_1, C and α for the different impedances are shown in Table 4.

The results reveal a very good fit for several vegetables and fruits. Fig. 16 presents the polar diagrams for the garlic, potato, tomato, kiwi and pear. It is clear that adopting circuits with more components, and other configuration, we can have better approximations. Therefore, in future development we will study new circuits for modeling the impedance of other materials.

Table 3. Characteristics of the vegetables and fruits

Vegetable or Fruit / Specie	Weight (kg)	Length (m)	Width (m)
Carrot / *Daucus Carota L.*	$8.85\ 10^{-2}$	$1.55\ 10^{-1}$	$3.39\ 10^{-2}$
Garlic / Allium sativum *L.*	$2.99\ 10^{-3}$	$1.38\ 10^{-2}$	$6.00\ 10^{-3}$
Onion / *Allium cepa L.*	$8.33\ 10^{-2}$	$5.86\ 10^{-2}$	$5.77\ 10^{-2}$
Potato / *Solanum tuberosum*	$1.24\ 10^{-1}$	$7.97\ 10^{-2}$	$5.99\ 10^{-2}$
Pimento / *Capsicum annuum*	$1.30\ 10^{-1}$	$1.23\ 10^{-1}$	$8.20\ 10^{-2}$
Tomato/*Lycopersicom esculentum*	$1.46\ 10^{-1}$	$5.57\ 10^{-2}$	$6.88\ 10^{-2}$
Turnip / *Brassica napobrassica*	$7.90\ 10^{-2}$	$7.26\ 10^{-2}$	$5.43\ 10^{-2}$
Apple / *Malus domestica*	$1.39\ 10^{-1}$	$6.36\ 10^{-2}$	$7.15\ 10^{-2}$
Banana / *Musa ingens*	$1.11\ 10^{-1}$	$1.49\ 10^{-1}$	$3.42\ 10^{-2}$
Kiwi / *Actinidia deliciosa*	$8.95\ 10^{-2}$	$6.52\ 10^{-2}$	$5.50\ 10^{-2}$
Lemon / *Citrus × limon*	$1.66\ 10^{-1}$	$9.19\ 10^{-2}$	$6.58\ 10^{-2}$
Orange / *Citrus sinensis*	$1.53\ 10^{-1}$	$6.69\ 10^{-2}$	$6.98\ 10^{-2}$
Pear / *Pyrus communis*	$9.72\ 10^{-2}$	$6.51\ 10^{-2}$	$5.63\ 10^{-2}$

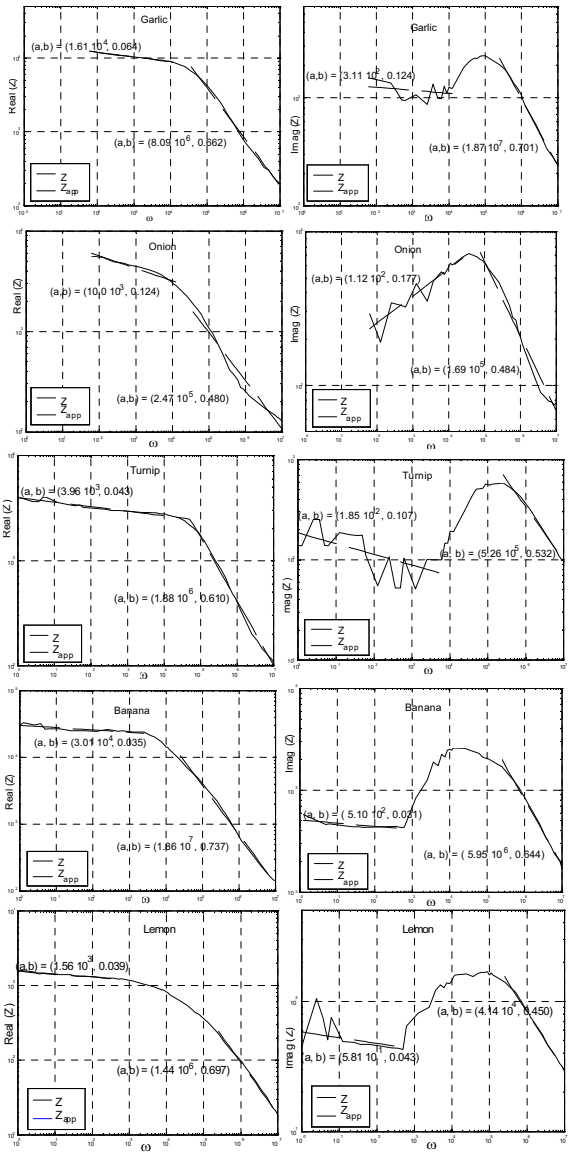

Fig. 14. Diagrams of real Re [$Z(j\omega)$] and imaginary Im [$Z(j\omega)$] parts of the electrical impedance for several vegetables and fruits: garlic (with $R_a = 15.0$ kΩ), onion (with $R_a = 2.7$ kΩ), turnip (with $R_a = 2.2$ kΩ), banana (with $R_a = 5.5$ kΩ) and lemon (with $R_a = 750$ Ω).

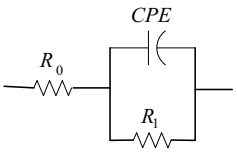

Fig. 15. The Randles circuit.

Table 4. Values of the elements of the Randles circuit for the garlic, potato, tomato, kiwi and pear

Vegetable / fruits	R_0 [Ω]	R_1 [Ω]	C	α
Garlic	1	$9.7\ 10^3$	$1.81\ 10^{-7}$	0.609
Potato	57	$3.15\ 10^3$	$2.40\ 10^{-7}$	0.677
Tomato	35.04	240.30	$5.00\ 10^{-6}$	0.565
Kiwi	28.04	242.00	$7.67\ 10^{-6}$	0.531
Pear	44.04	409.00	$1.14\ 10^{-6}$	0.619

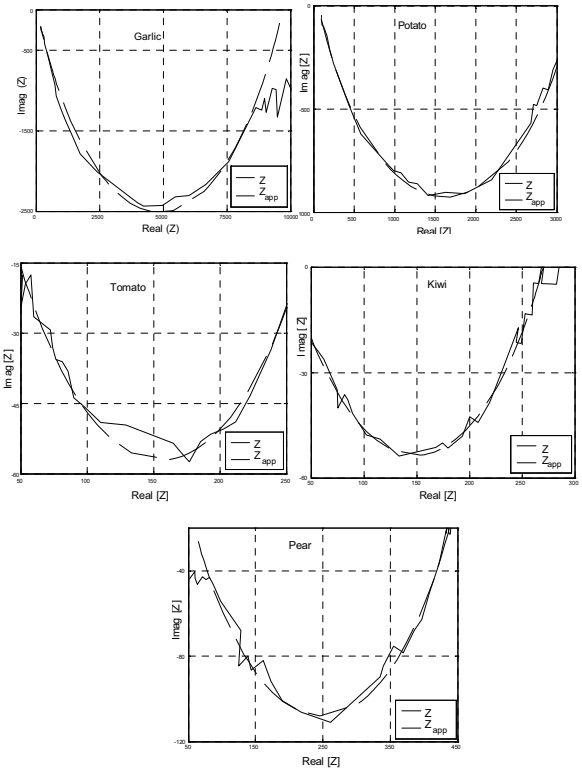

Fig. 16. Polar diagrams of the impedance $Z(j\omega)$ for several vegetables and fruits: garlic, potato tomato, kiwi and pear.

Recent research focus on the implementation of fractional order capacitances, often called fractances. Patents and commercial products are presently available, opening promising areas of application in electronics and control (Jesus *et al.*, 2006a).

This article follows an alternative strategy, studying natural living systems instead of technological artificial elements. Consequently, it points out interesting new directions towards the design of devices capable of measuring how mature is the fruit and vegetable, or to give an estimative of its life span for storage purposes.

5. IMPLEMENTATION OF THE FRACTIONAL POTENTIAL

The classical expressions for the electrical potential φ of a single charge, a dipole, a quadrupole, an infinite filament carrying a charge λ per unit length, two opposite charged filaments, and a planar surface with charge density σ reveal the relationship $\varphi \sim r^{-3}, r^{-2}, r^{-1}, \ln r, r$ (where r is the distance to the measuring point) corresponding to an integer-order differential relationship. Such state of affairs, motivated several authors to propose its generalization to fractional multipoles that produce a potential $\varphi \sim r^{-\alpha}, \alpha \in \Re$. Nevertheless, besides the abstract manipulation of mathematical expressions, the truth is that there is no practical method, and physical interpretation, for establishing the fractional potential (Jesus *et al.*, 2006b).

We start by re-evaluating the potential produced at point (x,y) by a straight filament with finite length l and charge q:

$$\varphi = \frac{1}{4\pi\varepsilon_0}\frac{q}{l}\ln\left\{\frac{y+\frac{1}{2}l+\sqrt{x^2+\left(y+\frac{1}{2}l\right)^2}}{y-\frac{1}{2}l+\sqrt{x^2+\left(y-\frac{1}{2}l\right)^2}}\right\}+C \quad (23)$$

It is well-known that for $x \to \infty$ we have $\varphi \to (q/4\pi\varepsilon_0)x^{-1}+C$ and, with $y = 0$, for $x \to 0$ we have $\varphi \to [q/(2\pi\varepsilon_0 l)]\ln(1/x)+C$. These limit cases correspond to a single charge and to an infinite filament.

We verify that expression (23) changes smoothly between the two limit cases. Therefore, we can have an intermediate fractional-order relationship as long as we restrict to a limited working range. This means that standard integer-order potential relationships have a global nature while fractional-order potentials have a local nature possible to capture only in a restricted region. This conclusion leads to an approximation scheme based on a recursive placement of integer-order functions.

In this line of thought, we developed a one-dimensional GA that places recursively n charges q_i ($i = 0, \ldots, (n-1)/2$, n–odd; $i = 1, \ldots, n/2$, n–even) at the symmetrical positions $\pm x_i$, with exception of $x_0 = 0$ that corresponds to the centre of the n-array of charges where there is a single charge q_0.

Our goal is to compare the desired reference potential $\varphi_{ref} = kx^{\alpha}$, with the approximate potential φ_{app}, resulting from a number n of charges q_i located at x_i, given by:

$$\begin{cases} \varphi_{app} = \dfrac{q_0}{|x|}+\displaystyle\sum_{i=1}^{\frac{n-1}{2}}\frac{q_i}{4\pi\varepsilon_0}\left(\frac{1}{|x-x_i|}+\frac{1}{|x+x_i|}\right), & n \text{ odd} \\ \varphi_{app} = \displaystyle\sum_{i=1}^{\frac{n}{2}}\frac{q_i}{4\pi\varepsilon_0}\left(\frac{1}{|x-x_i|}+\frac{1}{|x+x_i|}\right), & n \text{ even} \end{cases} \quad (24)$$

The experiments consist on executing the GA, for generating a combination of positions and charges that lead to an electrical potential with fractional slope similar to the desire reference potential. The values of GA parameters are: population number P = 40, crossover C(%) = 85.0%, mutation M(%) = 1.0%, elitist strategy ES(%) = 10.0% and a maximum number of generations G = 100. The optimization fitness function corresponds to the minimization of the error:

$$J = \sum_{k=1}^{m}\left(\ln|\varphi_{app}/\varphi_{ref}|\right)^2, \quad \min_i(J), \quad i = 0, 1, \ldots, n-1 \quad (25)$$

where m is the number of sampling points along the x-axis.

In the present case, we consider a log-log perspective, but its modification for a lin-lin case is straightforward.

For example, Fig. 17 shows φ_{app} for an approximation with $n = 5$ charges, when $\varphi_{ref} = 1.0x^{-1.5}$ and $0.2 < x < 0.8$.

After 32 iterations the GA leads to $q_{0A} = -0.489$ [volt], $q_{1A} = 0.920$ [volt] and $q_{2A} = -0.077$ [volt] (with scale factor $\times (4\pi\varepsilon_0)^{-1}$), at $x_{0A} = 0.0$ [m], $x_{1A} = \pm 0.147$ [m] and $x_{2A} = \pm 0.185$ [m], respectively.

The results show a good fit between the two functions. Executing the GA several times we verify that it is possible to find more than one 'good' solution. For a given application, a superior precision may be required and, in that case, a larger number of charges must be used. In this line of thought, we study the precision of this method for different number of charges, namely from $n = 1$ up to $n = 10$ charges.

Figure 17 depicts the minimum, maximum and average of J versus n, to achieve a valid solution for a statistical sample of 10 GA executions. This chart confirms that we have a better precision the larger the number of charges. Also, the results reveal the requirement of a larger number of iterations when the number of charges increases, and consequently a larger calculation time.

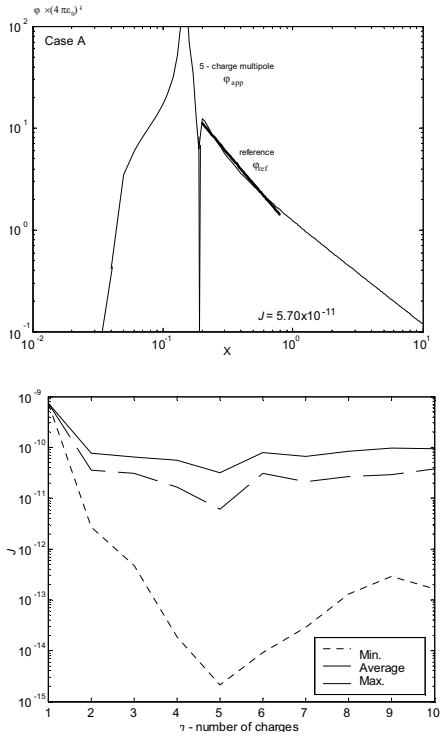

Fig. 17. Comparison of the electric potential φ_{app} and $\varphi_{ref} = 1.0x^{-1.5}$ [volt] *vs.* x for $0.2 < x < 0.8$ [m] and $n = 5$ and the corresponding approximation error J *vs.* number charges n.

We verify also that the position of the charges varies significantly with the number of charges used in the approximation. Therefore, pattern of the charge *versus* the location is not clear and its comparison with a fractal recursive layout is still under investigation.

6. FRACTIONAL DYNAMICS IN THE TRAJECTORY CONTROL OF REDUNDANT MANIPULATORS

A kinematically redundant manipulator is a robotic arm possessing more degrees of freedom (*dof*) than those required to establish an arbitrary position and orientation of the gripper. Redundant manipulators offer several potential advantages over non-redundant arms. In a workspace with obstacles, the extra degrees of freedom can be used to move around or between obstacles and thereby to manipulate in situations that otherwise would be inaccessible (Klein and Huang, 1983; Yoshikawa, 1988; Conkur and Buckingham, 1997; Chiaverini, 1997).

When a manipulator is redundant, it is anticipated that the inverse kinematics admits an infinite number of solutions. This implies that, for a given location of the manipulator's gripper, it is possible to induce a self-motion of the structure without changing the location of the end effecter. Therefore, the arm can be reconfigured to find better postures for an assigned set of task requirements.

Several kinematic techniques for redundant manipulators control the gripper through the rates at which the joints are driven, using the pseudoinverse of the Jacobian (Conkur and Buckingham, 1997; Bay, 1992). Nevertheless, these algorithms lead to a kind of chaotic motion with unpredictable arm configurations.

6.1 Kinematics of Redundant Manipulators

A kinematically redundant manipulator is a robotic arm possessing more *dof* than those required to establish an arbitrary position and orientation of the gripper. In Fig. 18 is depicted a planar manipulator with $k \in \aleph$ rotational (R) joints that is redundant for $k > 2$. When a manipulator is redundant it is anticipated that the inverse kinematics admits an infinite number of solutions. This implies that, for a given location of the manipulator's gripper, it is possible to induce a self-motion of the structure without changing the location of the gripper. Therefore, redundant manipulators can be reconfigured to find better postures for an assigned set of task requirements but, on the other hand, have a more complex structure requiring adequate control algorithms.

We consider a manipulator with n degrees of freedom whose joint variables are denoted by $\mathbf{q} = [q_1, q_2, ..., q_n]^T$. We assume that a class of tasks we are interested in can be described by m variables, $\mathbf{x} = [x_1, x_2, ..., x_m]^T$ ($m < n$) and that the relation between $\mathbf{q}$ and $\mathbf{x}$ is given by:

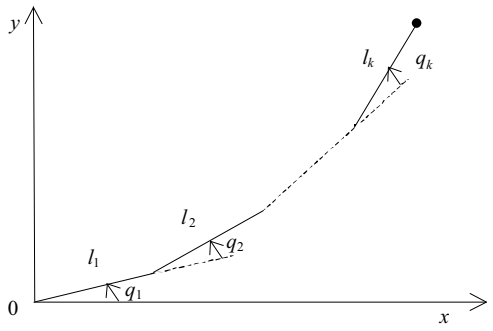

Fig. 18. A planar redundant planar manipulator with k rotational joints.

$$\mathbf{x} = f(\mathbf{q}) \tag{26}$$

where f is a function representing the direct kinematics.

Differentiating (26) with respect to time yields:

$$\dot{\mathbf{x}} = \mathbf{J}(\mathbf{q})\dot{\mathbf{q}} \tag{27}$$

where $\dot{\mathbf{x}} \in \Re^m$, $\dot{\mathbf{q}} \in \Re^n$ and $\mathbf{J}(\mathbf{q}) = \partial f(\mathbf{q})/\partial \mathbf{q} \in \Re^{m \times n}$. Hence, it is possible to calculate a path $\mathbf{q}(t)$ in terms of a prescribed trajectory $\mathbf{x}(t)$ in the operational space. We assume that the following condition is satisfied:

$$\max \text{ rank } \{\mathbf{J}(\mathbf{q})\} = m \tag{28}$$

Failing to satisfy this condition usually means that the selection of manipulation variables is redundant and the number of these variables m can be reduced. When condition (27) is verified, we say that the degree of redundancy of the manipulator is $n–m$. If, for some $\mathbf{q}$ we have:

$$\text{rank } \{\mathbf{J}(\mathbf{q})\} < m \tag{29}$$

then the manipulator is in a singular state. This state is not desirable because, in this region of the trajectory, the manipulating ability is very limited.

Many approaches for solving redundancy (Doty *et al.*, 1993; Roberts and Maciejewski, 1994) are based on the inversion of equation (27). A solution in terms of the joint velocities is sought as:

$$\dot{\mathbf{q}} = \mathbf{J}^{\#}(\mathbf{q})\dot{\mathbf{x}} \tag{30}$$

where $\mathbf{J}^{\#}$ is one of the generalized inverses of the $\mathbf{J}$ (Siciliano, 1990; Nakamura, 1991; Doty *et al.*, 1993). It can be easily shown that a more general solution to equation (27) is given by:

$$\dot{\mathbf{q}} = \mathbf{J}^{+}(\mathbf{q})\dot{\mathbf{x}} + \left[\mathbf{I} - \mathbf{J}^{+}(\mathbf{q})\mathbf{J}(\mathbf{q})\right]\dot{\mathbf{q}}_0 \tag{31}$$

where $\mathbf{I}$ is the $n \times n$ identity matrix and $\dot{\mathbf{q}}_0 \in \Re^n$ is a $n \times 1$ arbitrary joint velocity vector and $\mathbf{J}^{+}$ is the pseudoinverse of the $\mathbf{J}$. The solution (31) is composed of two terms. The first term is relative to minimum norm joint velocities. The second term, the

homogeneous solution, attempts to satisfy the additional constraints specified by $\dot{\mathbf{q}}_0$. Moreover, the matrix $\mathbf{I}-\mathbf{J}^{+}(\mathbf{q})\mathbf{J}(\mathbf{q})$ allows the projection of $\dot{\mathbf{q}}_0$ in the null space of **J**. A direct consequence is that it is possible to generate internal motions that reconfigure the manipulator structure without changing the gripper position and orientation (Siciliano, 1990; Doty *et al.*, 1993; Chung *et al.*, 1994; Seereeram and Wen, 1995). Another aspect revealed by the solution of (30) is that repetitive trajectories in the operational space do not lead to periodic trajectories in the joint space. This is an obstacle for the solution of many tasks because the resultant robot configurations have similarities with those of a chaotic system.

6.2 Robot Trajectory Control

The direct kinematics and the Jacobian of a 3-link planar manipulator with rotational joints (3*R* robot) has a simple recursive nature according with the expressions:

$$\begin{bmatrix} x \\ y \end{bmatrix} = \begin{bmatrix} l_1 C_1 + l_2 C_{12} + l_3 C_{123} \\ l_1 S_1 + l_2 S_{12} + l_3 S_{123} \end{bmatrix} \tag{32a}$$

$$\mathbf{J} = \begin{bmatrix} -l_1 S_1 - \ldots - l_3 S_{123} & \ldots & -l_3 S_{123} \\ l_1 C_1 + \ldots + l_3 C_{123} & \ldots & l_3 C_{123} \end{bmatrix} \tag{32b}$$

where l_i is the length of link i, $q_{i\ldots k} = q_i + \ldots + q_k$, $S_{i\ldots k} = Sin(q_{i\ldots k})$ and $C_{i\ldots k} = Cos(q_{i\ldots k})$.

During all the experiments it is considered $\Delta t = 10^{-3}$ sec, $L_{TOT} = l_1 + l_2 + l_3 = 3$ and $l_1 = l_2 = l_3$.

In the closed-loop pseudoinverse's method the joint positions can be computed through the time integration of the velocities according with the block diagram of the inverse kinematics algorithm depicted in Fig. 19 where $\mathbf{x_{ref}}$ represents the vector of reference coordinates of the robot gripper in the operational space.

Based on equation (32) we analyze the kinematic performances of the 3*R*-robot when repeating a circular motion in the operational space with frequency $\omega_0 = 7.0$ rad sec^{-1}, centre at distance $r = [x^2+y^2]^{1/2}$ and radius ρ.

Figure 20 show the joint positions for the inverse kinematic algorithm (17) for r = {0.6, 2.0} and ρ = {0.3, 0.5}. We observe that:

- For r = 0.6 occur unpredictable motions with severe variations that lead to high joint transients (Duarte *et al.*, 2002). Moreover, we verify a low frequency signal modulation that depends on the circle being executed.
- For r = 2.0 the motion is periodic with frequency identical to $\omega_0 = 7.0$ rad sec^{-1}.

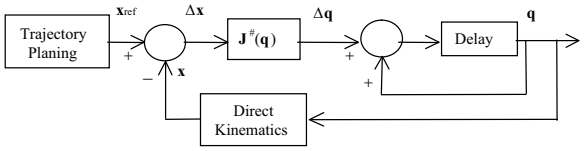

Fig. 19. Block diagram of the closed-loop inverse kinematics algorithm with the pseudoinverse.

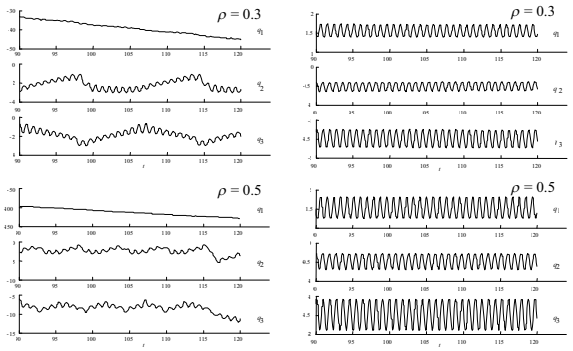

Fig. 20. The 3*R*-robot joint positions *versus* time using the pseudoinverse method for r = {0.6, 2.0} and ρ = {0.3, 0.5}.

6.3 Robot Analysis of the Robot Trajectories

In the previous section we verified that the pseudoinverse based algorithm leads to unpredictable arm configurations. In order to gain further insight into the pseudoinverse nature several distinct experiments are devised in the sequel during a time window of 300 cycles. Therefore, in a first set of experiments we calculate the Fourier transform of the 3*R*-robot joints velocities for a circular repetitive motion with frequency ω_0 = 7.0 rad sec^{-1}, radius ρ= {0.1, 0.3, 0.5, 0.7} and radial distances $r \in]0, L_{TOT} - \rho[$.

Figures 21-24 show $\left|F\{\dot{q}_2(t)\}\right|$ *versus* the frequency ratio ω_0/ω and the distance r where $F\{\ \}$ represents the Fourier operator. Is verified an interesting phenomenon induced by the gripper repetitive motion ω_0 because a large part of the energy is distributed along several sub-harmonics. These fractional order harmonics (*foh*) depend on r and ρ making a complex pattern with similarities with those revealed by chaotic systems. Furthermore, we observe the existence of several distinct regions depending on r.

For example, selecting in Fig. 24 several distinct cases, namely for r = {0.08, 0.30, 0.53, 1.10, 1.30, 2.00}, we have the different signal Fourier spectra clearly visible in Fig. 25. Joints 1 and 3 show similar velocity spectra.

In the author's best knowledge the *foh* are aspects of fractional dynamics (Machado, 1997, 2001; Marcos *et al.*, 2007), but a final and assertive conclusion about a physical interpretation is a matter still to be explored.

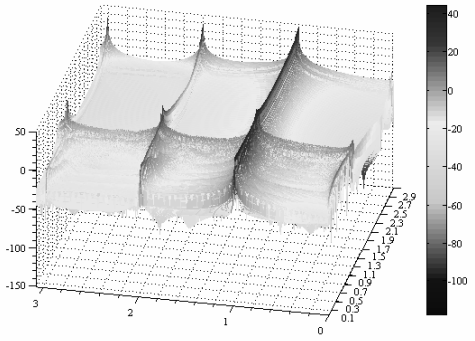

Fig. 21. $\left|F\left\{\dot{q}_2(t)\right\}\right|$ of the 3*R*-robot during 300 cycles, vs r and ω/ω_0, for $\rho = 0.1$, $\omega_0 = 7.0$ rad $\sec^{-1}$.

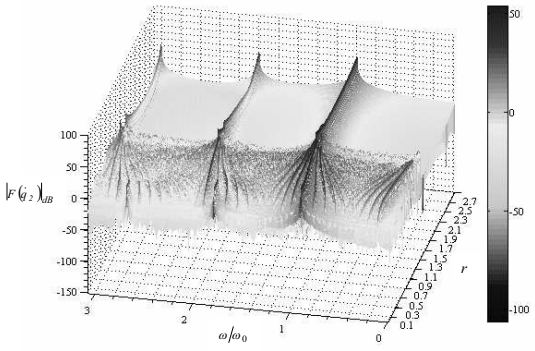

Fig. 22. $\left|F\left\{\dot{q}_2(t)\right\}\right|$ of the 3*R*-robot during 300 cycles, vs r and ω/ω_0, for $\rho = 0.3$, $\omega_0 = 7.0$ rad $\sec^{-1}$.

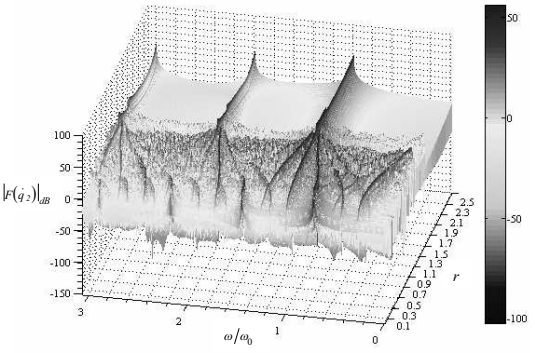

Fig. 23. $\left|F\left\{\dot{q}_2(t)\right\}\right|$ of the 3*R*-robot during 300 cycles, vs r and ω/ω_0, for $\rho = 0.5$, $\omega_0 = 7.0$ rad $\sec^{-1}$.

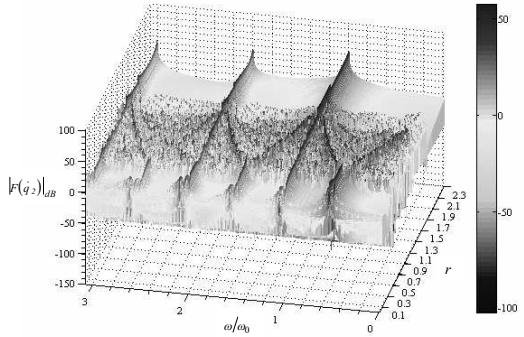

Fig. 24. $\left|F\left\{\dot{q}_2(t)\right\}\right|$ of the 3*R*-robot during 300 cycles, vs r and ω/ω_0, for $\rho = 0.7$, $\omega_0 = 7.0$ rad $\sec^{-1}$.

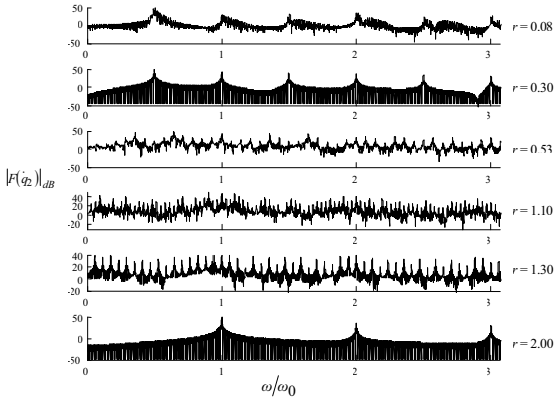

Fig. 25. $\left|F\left\{\dot{q}_2(t)\right\}\right|$ of the 3*R*-robot during 300 cycles, vs the frequency ratio ω/ω_0, for r = {0.08, 0.30, 0.53, 1.10, 1.30, 2.00}, $\rho = 0.7$, $\omega_0 = 7.0$ rad $\sec^{-1}$.

For joints velocities 1 and 3 the results are similar to the verified ones for joint velocity 2.

7. FRACTIONAL ORDER FOURIER SPECTRA IN ROBOTIC MANIPULATORS WITH VIBRATIONS

This section presents a fractional calculus (FC) perspective in the study of the robotic signals captured during an impact phase of the manipulator. In the experiment is used a steel rod flexible link. To test impacts, the link consists on a long, thin, round, flexible steel rod clamped to the end-effector of the manipulator. The robot motion is programmed in a way such that the rod moves against a rigid surface. During the motion of the manipulator the clamped rod is moved by the robot against a rigid surface. An impact occurs and several signals are recorded with a sampling frequency of $f_s = 500$ Hz. In order to analyze the vibration and impact phenomena an acquisition system was developed (Lima *et al.*, 2005). The instrumentation system acquires signals from multiple sensors that capture the axis positions, mass accelerations, forces and moments and electrical currents in the motors. Afterwards, an analysis package, running off-line, reads the data recorded by the acquisition system and examines them. Due to space limitations only some of the signals are depicted. A typical time evolution of the electrical currents of robot axis motors is shown in Fig. 26 corresponding to: (*i*) the impact of the rod on a rigid surface and (*ii*) without impact (Lima *et al.*, 2006). In this example, the signals present clearly a strong variation at the instant of the impact that occurs, approximately, at $t = 4$ sec.

In order to study the behavior of the signal Fourier transform, a trendline can be superimposed over the spectrum based on a power law approximation:

$$\left|\mathrm{F}\left\{f(t)\right\}\right| \approx c\omega^m \tag{33}$$

where F{} is Fourier operator, c is a constant, ω is the frequency and m is the slope.

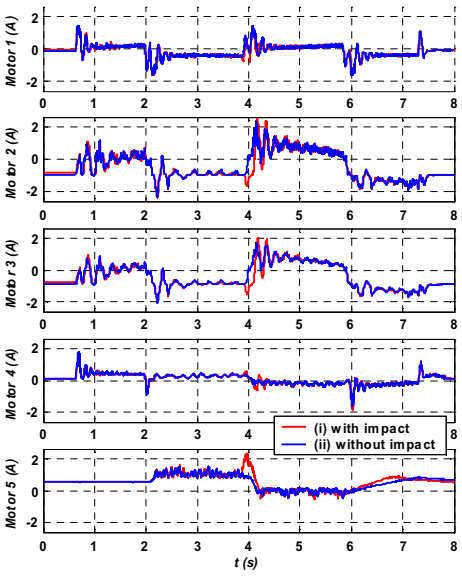

Fig. 26. Electrical currents of robot axis motors.

Figure 27 shows the amplitude of the Fast Fourier Transform (FFT) of the axis 1 position signal. The trendline (33) leads to a slope $m = -0.99$ revealing, clearly, the integer order behavior. The others position signals were studied, revealing also an integer behavior, both under impact and no impact conditions.

Figure 28 shows the amplitude of the FFT of the electrical current for the axis 3 motor. The spectrum was also approximated by trendlines in a frequency range larger than one decade. These trendlines (Fig. 28) have slopes of $m = -1.52$ and $m = -1.51$ under impact (*i*) and without impact (*ii*) conditions, respectively. The lines present a fractional order behavior in both cases. The others axis motor currents were studied, as well. Some of them, for a limited frequency range, present also fractional order behavior while others have a complicated spectrum difficult to approximate by one trendline.

Figure 29 shows, as example, the spectrum of the F_z force. This spectrum is not so well defined in a large frequency range. All force/moments spectra present identical behavior and, therefore, it is difficult to define accurately the behavior of the signals.

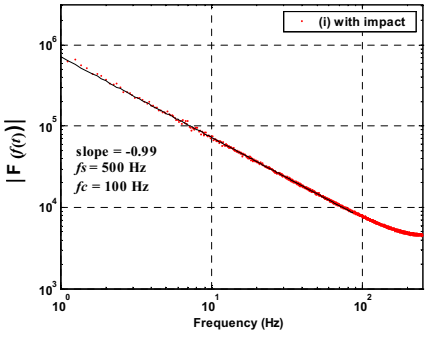

Fig. 27. Spectrum of the axis 1 position.

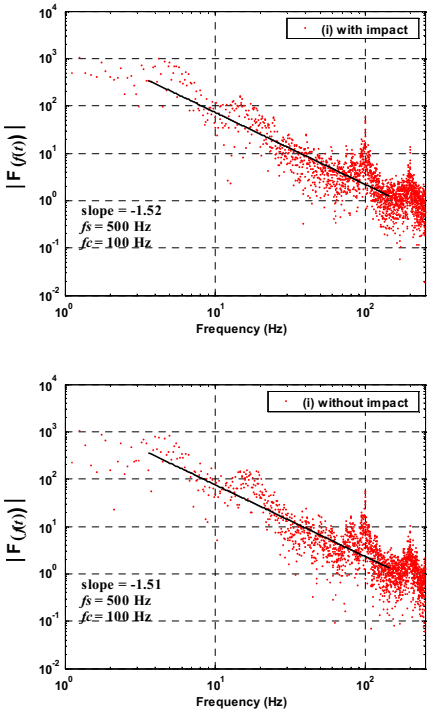

Fig. 28. Spectrum of the axis 3 motor current.

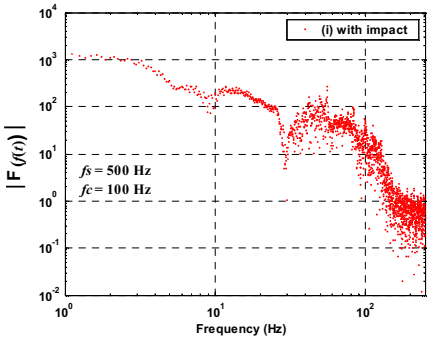

Fig. 29. F_z force spectrum with impact.

Finally, Fig. 30 depicts the spectrum of the signal captured from the accelerometer 1 located at the rod free-end of the beam. Like the spectrum from the other accelerometer located at the rod clamped-end, this spectrum is spread and complicated. Therefore, it is difficult to define accurately the slope of the signal and consequently its behavior in terms of integer or fractional system.

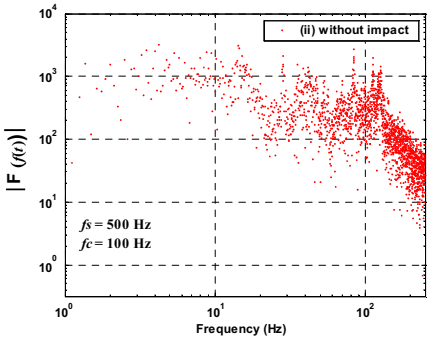

Fig. 30. Acceleration spectrum of the rod free-end without impact.

As shown in the examples, the Fourier spectrum of several signals, captured during an impact phase of the manipulator, presents a non integer behavior. On the other hand, the feedback fractional order systems, due to the success in the synthesis of real noninteger differentiator and the emergence of fractional-order controllers (Barbosa *et al.*, 2004), have been designed and applied to control a variety of dynamical processes (Oustaloup *et al.*, 1997). Therefore the study presented here can assist in the design of the control system to be used in eliminating or reducing the effect of vibrations.

8. STOCK PRICING DYNAMICS

In this section are studied daily records of international stock prices (Peters, 1996; Ramirez *et al.*, 2002) using the Fourier transform and the Pseudo Phase Plane (*PPP*). It is analysed the unpredictability based on the power law of the decay of the Fourier transform. Several examples show the evidence that the S&P 500 Stock market is a persistent process, with long-run memory effects.

8.1 Spectral Analysis of Market Indices

Several signals $x_i(t)$, $i \in \aleph$, ranging from 7910 trading-days in the same time period, were selected from the pool of the 500 biggest companies in US.

The Fourier transform is a mathematical tool (Szu, 1984) well adapted for analyzing the dynamics of the financial indices. The Fourier spectra $\mathrm{F}\{x_i(t)\}$ reveal a power decay that can be approximated by:

$$|\mathrm{F}\{x_i(t)\}| \approx c\ \omega^m,\ i \in \aleph,\ c,m \in \Re \qquad (34)$$

Figures 31 and 32 show the time series for three cases, and the corresponding Fourier transform with the approximation formula (34) that characterizes the decay slope, respectively. Table 5 depicts the ticker of the financial index and the corresponding spectral slopes *m*.

In Fig. 32 are also displayed the values of R^2, the square of the correlation factor between $ln(\omega)$ and $ln|\mathrm{F}\{x\}|$, that reflects the degree of statistical association of the pair of variables.

Figure 33 shows the relation between *m* and R^2, revealing that this association is almost functional.

8.2 Pseudo Phase Plane Analysis

The *PPP* is a tool that makes easier the study of the time series dynamics by its representation in a 2D space (Liebovitch, 1998; Feeny, 2004).

Table 5. Characteristics of five financial indices

Ticker	*m*	dim_{PPP}	*d*
F0	–0.7790	1.463	1062
HPQ0	–0.8849	1.435	697
SUN0	–1.003	1.642	545
CTL0	–1.108	1.379	919
ECL0	–1.223	1.415	1043

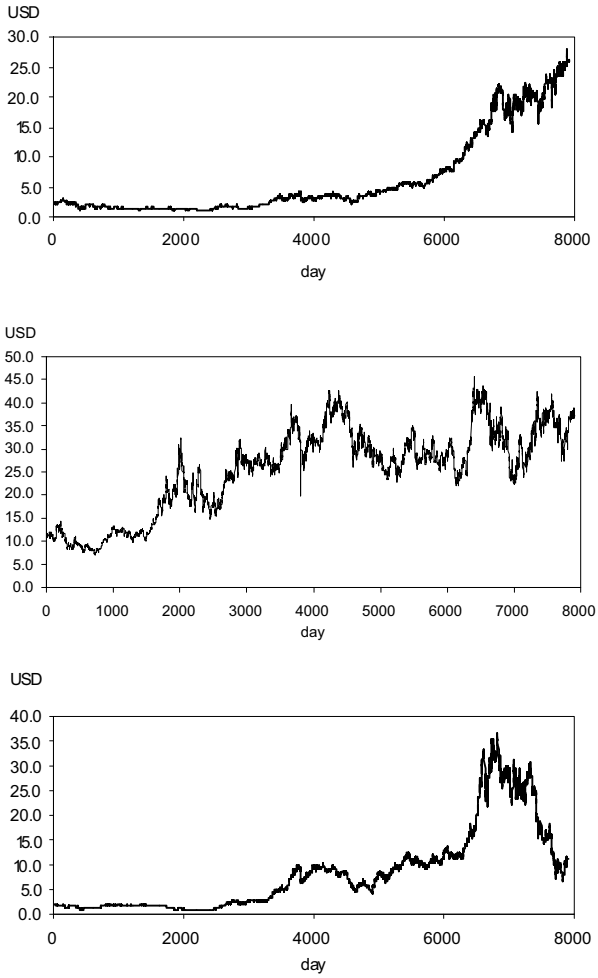

Fig. 31. Plots of the time series of the financial indices ECL0, SUN0 and F0.

Once a delay *d* is selected the *PPP* is a plot of the points:

$$P_d = \left\{(x_t, x_{t+d}) \in R^2 : t = 0,1,\cdots,N-d, 0 < d < N\right\} \qquad (35)$$

A process, based on information theory, to determine the delay *d* that provides the best candidate for periodicity was proposed by (Trendafilova and Brussel, 2001; Feeny, 2004). Several experiments revealed that an alternative, but simpler, way for selecting the delay is based in detecting the first contrasting minimum in the autocorrelation function (*ACF*) witch can be defined by the expression:

$$ACF(d) = \sum_{t=d}^{n}(x_t - \bar{x})(x_{t+d} - \bar{x}) \Big/ \sum_{t=d}^{n}(x_t - \bar{x})^2 \qquad (36)$$

As a drawback, this equivalent process must be done with the user supervision because, sometimes, due to the noise embedded in some financial signals the first minimum proposed by the computer program is not sufficient clear, and therefore must be seen as a false minimum.

In Fig. 34 are plotted the *ACF*s of three signals showing the first contrasting minima. The resulting *PPP*s are also represented and their fractal dimension dim_{PPP} is calculated (Fig. 35).

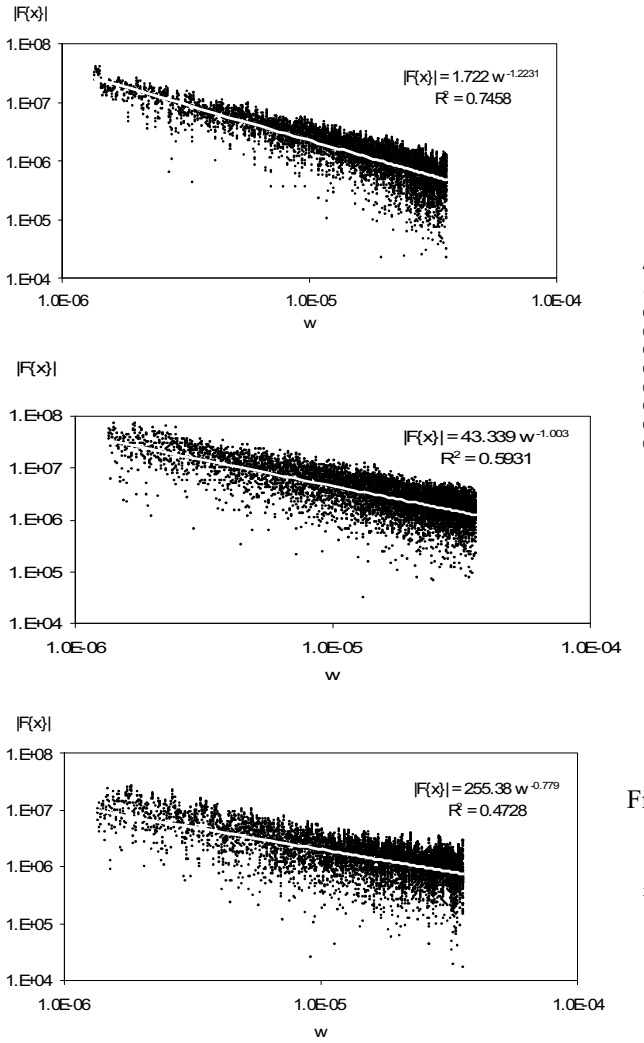

Fig. 32. Plots of the Fourier transform of the financial indices ECL0, SUN0 and F0.

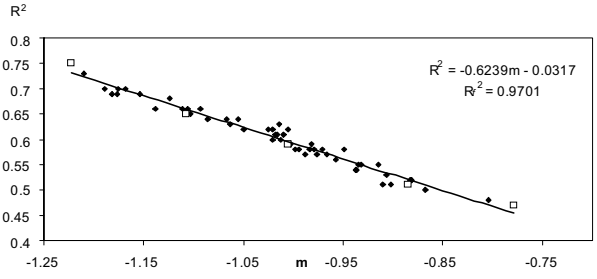

Fig. 33. Plot of the decay slope *m versus* the correlation coefficient R^2 of the previous charts of the Fourier transform for several financial indices. The square marks represent the position of the five specific tickers under study.

The results reveal that the delay *d*, required for the *PPP* representation, and the fractal dimension dim_{PPP} (Falconer, 2003) have a minimum and a maximum, respectively, when $m = -1$. A preliminary analysis indicates that this behavior is related with the unpredictable of the time series and to the nature of phenomena similar to biased random walks. A deeper understanding of the fractional or integer value of *d*, the fractal characteristics of the *PPP* and the signal predictability needs to be further explored.

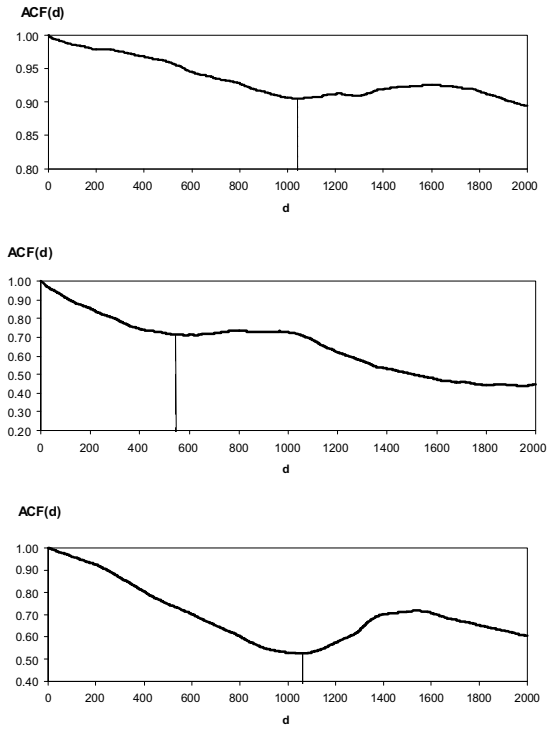

Fig. 34. Plots of the *ACF* for the financial indices ECL0, SUN0 and F0.

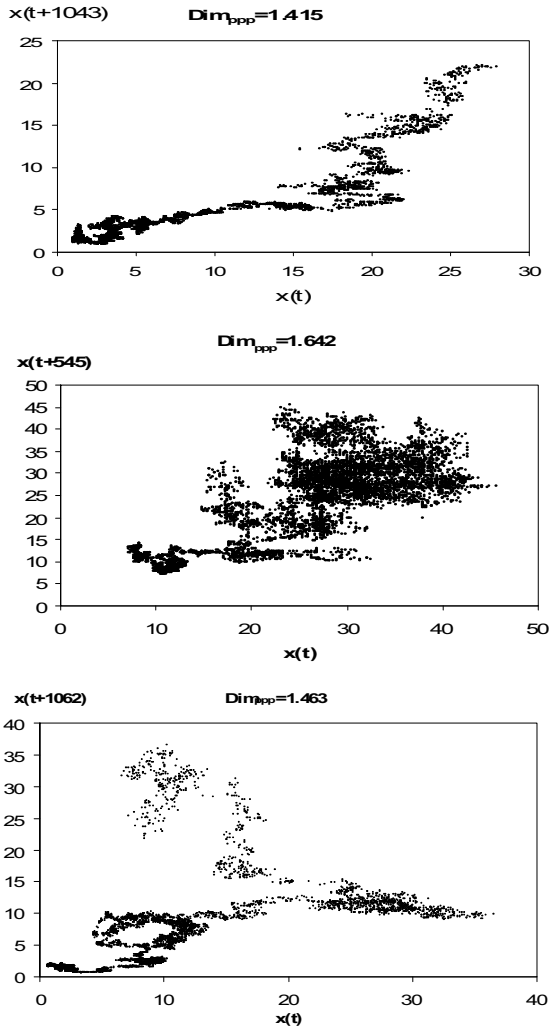

Fig. 35. Plot of the *PPP* for the financial indices ECL0, SUN0 and F0.

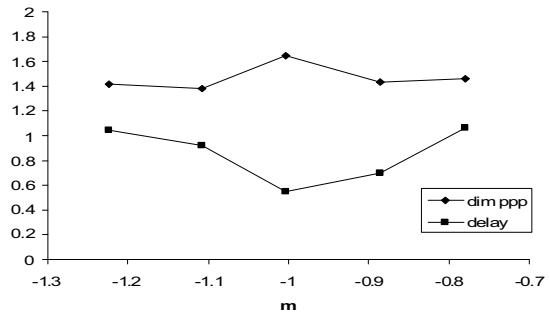

Fig. 36. Plots of dim_{PPP} and d *versus* m.

Table 5 suggests a relationship between m, dim_{PPP} and d. These characteristics are clearly depicted in Fig. 36.

9. CIRCUIT SYNTHESIS USING EVOLUTIONARY ALGORITHMS

In recent decades evolutionary computation (EC) techniques have been applied to the design of electronic circuits and systems, leading to a novel area of research called Evolutionary Electronics (EE) or Evolvable Hardware (EH). EE considers the concept for automatic design of electronic systems. Instead of using human conceived models, abstractions and techniques, EE employs search algorithms to develop implementations not achievable with the traditional design schemes, such as the Karnaugh or the Quine-McCluskey Boolean methods.

Several papers proposed designing combinational logic circuits using evolutionary algorithms and, in particular, genetic algorithms (GAs) (Goldberg, 1989; Louis and Designer, 1991) and hybrid schemes such as the memetic algorithms (MAs) (Reis *et al.*, 2005a).

Particle swarm optimization (PSO) constitutes an alternative evolutionary computation technique, and this paper studies its application to combinational logic circuit synthesis.

9.1 Particle Swarm Optimization

In the literature about PSO the term 'swarm intelligence' appears rather often and, therefore, we begin by explaining why this is so.

Non-computer scientists (ornithologists, biologists and psychologists) did early research, which led into the theory of particle swarms. In these areas, the term 'swarm intelligence' is well known and characterizes the case when a large number of individuals are able of accomplish complex tasks. Motivated by these facts, some basic simulations of swarms were abstracted into the mathematical field. The usage of swarms for solving simple tasks in nature became an intriguing idea in algorithmic and function optimization.

Eberhart and Kennedy were the first to introduce the PSO algorithm (Kennedy and Eberhart, 1995), which is an optimization method inspired in the collective intelligence of swarms of biological populations, and was discovered through simplified social model simulation of bird flocking, fishing schooling and swarm theory.

In the PSO, instead of using genetic operators, as in the case of GAs, each particle (individual) adjusts its flying according with its own and its companions experiences. Each particle is treated as a point in a D-dimensional space and is manipulated as described below in the original PSO algorithm:

$$v_{id} = v_{id} + c_1 rand()(p_{id} - x_{id}) + c_2 Rand()(p_{gd} - x_{id}) \quad (37a)$$

$$x_{id} = x_{id} + v_{id} \quad (37b)$$

where c_1 and c_2 are positive constants, *rand*() and *Rand*() are two random functions in the range [0,1], $X_i = (x_{i1}, x_{i2}, \ldots, x_{iD})$ represents the i^{th} particle, $P_i = (p_{i1}, p_{i2}, \ldots, p_{iD})$ is the best previous position (the position giving the best fitness value) of the particle, the symbol g represents the index of the best particle among all particles in the population, and $V_i = (v_{i1}, v_{i2}, \ldots, v_{iD})$ is the rate of the position change (velocity) for particle i.

Expression (37) represents the flying trajectory of a population of particles. Equation (37a) describes how the velocity is dynamically updated and equation (37b) the position update of the "flying" particles. Equation (37a) is divided in three parts, namely the momentum, the cognitive and the social parts. In the first part the velocity cannot be changed abruptly: it is adjusted based on the current velocity. The second part represents the learning from its own flying experience. The third part consists on the learning group flying experience (Shi and Eberhart, 1998).

The first new parameter added into the original PSO algorithm is the inertia weigh. The dynamic equation of PSO with inertia weigh is modified to be:

$$v_{id} = wv_{id} + c_1 rand()(p_{id} - x_{id}) + c_2 Rand()(p_{gd} - x_{id}) \quad (38a)$$

$$x_{id} = x_{id} + v_{id} \quad (38b)$$

where w constitutes the inertia weigh that introduces a balance between the global and the local search abilities. A large inertia weigh facilitates a global search while a small inertia weigh facilitates a local search.

Another parameter, called constriction coefficient k, is introduced with the hope that it can insure a PSO to converge. A simplified method of incorporating it appears in equation (38), where k is function of c_1 and c_2 as it is presented in equation (39).

$$v_{id} = k\left[v_{id} + c_1 rand()(p_{id} - x_{id}) + c_2 Rand()(p_{gd} - x_{id})\right] \quad (39a)$$

$$x_{id} = x_{id} + v_{id} \quad (39b)$$

$$k = 2\left(2 - \phi - \sqrt{\phi^2 - 4\phi}\right)^{-1} \quad (39c)$$

where $\phi = c_1 + c_2$, $\phi > 4$.

There are two different PSO topologies, namely the global version and the local version. In the global version of PSO, each particle flies through the search space with a velocity that is dynamically adjusted according to the particle's personal best performance achieved so far and the best performance achieved so far by all particles. On the other hand, in the local version of PSO, each particle's velocity is adjusted according to its personal best and the best performance achieved so far within its neighborhood. The neighborhood of each particle is generally defined as topologically nearest particles to the particle at each side.

PSO is an evolutionary algorithm simple in concept, easy to implement and computationally efficient. Figs. 37-39 present a generic EC algorithm, a hybrid algorithm, more precisely a MA and the original procedure for implementing the PSO algorithm, respectively.

The different versions of the PSO algorithms are: the real-value PSO, which is the original version of PSO and is well suited for solving real-value problems; the binary version of PSO, which is designed to solve binary problems; and the discrete version of PSO, which is good for solving the event-based problems. To extend the real-value version of PSO to binary/discrete space, the most critical part is to understand the meaning of concepts such as trajectory and velocity in the binary/discrete space.

Kennedy and Eberhart (1995) use velocity as a probability to determine whether x_{id} (a bit) will be in one state or another (zero or one). The particle swarm formula of equation (37a) remains unchanged, except that now p_{id} and x_{id} are integers in [0.0,1.0] and a logistic transformation $S(v_{id})$ is used to accomplish this modification. The resulting change in position is defined by the following rule:

$$if\ [rand() < S(v_{id})] \quad then\ x_{id} = 1;\ \ else\ x_{id} = 0 \quad (40)$$

where the function $S(v)$ is a sigmoid limiting transformation and $rand()$ is a random number selected from a uniform distribution in the range [0.0,1.0].

1. Initialize the population
2. Calculate the fitness of each individual in the population
3. Reproduce selected individuals to form a new population
4. Perform evolutionary operations such as crossover and mutation on the population
5. Loop to step 2 until some condition is met

Fig. 37. Evolutionary computation algorithm.

1. Initialize the population
2. Calculate the fitness of each individual in the population
3. Reproduce selected individuals to form a new population
4. Perform evolutionary operations such as crossover and mutation on the population
5. Apply a local search algorithm
5. Loop to step 2 until some condition is met

Fig. 38. Memetic algorithm.

1. Initialize population in hyperspace
2. Evaluate fitness of individual particles
3. Modify velocities based on previous best and global (or neighborhood) best
4. Terminate on some condition
5. Go to step 2

Fig. 39. Particle swarm optimization process.

9.2 PSO Based Circuit Design

We adopt a PSO algorithm to design combinational logic circuits. A truth table specifies the circuits and the goal is to implement a functional circuit with the least possible complexity. Four sets of logic gates have been defined, as shown in Table 6, being *Gset 2* the simplest one (*i.e.*, a RISC-like set) and *Gset 6* the most complex gate set (*i.e.*, a CISC-like set). Logic gate named WIRE means a logical no-operation.

In the PSO scheme the circuits are encoded as a rectangular matrix **A** ($row \times column = r \times c$) of logic cells as represented in Fig. 40. Three genes represent each cell: *<input1><input2><gate type>*, where *input1* and *input2* are one of the circuit inputs, if they are in the first column, or one of the previous outputs, if they are in other columns. The gate type is one of the elements adopted in the gate set. The chromosome is formed with as many triplets as the matrix size demands (*e.g.*, triplets = $3 \times r \times c$). For example, the chromosome that represents a 3×3 matrix is depicted in Fig. 41.

The initial population of circuits (particles) has a random generation. The initial velocity of each particle is initialized with zero. The following velocities are calculated applying equation (38a) and the new positions result from using equation (38b). In this way, each potential solution, called particle, flies through the problem space. For each gene is calculated the corresponding velocity. Therefore, the new positions are as many as the number of genes in the chromosome. If the new values of the input genes result out of range, then a re-insertion function is used. If the calculated gate gene is not allowed a new valid one is generated at random. These particles then have memory and each one keeps information of its previous best position (*pbest*) and its corresponding fitness. The swarm has the pbest of all the particles and the particle with the greatest fitness is called the global best (*gbest*).

Table 6. Gate sets

Gate Set	Logic gates
Gset 2	{AND,XOR,WIRE}
Gset 3	{AND,OR,XOR,WIRE}
Gset 4	{AND,OR,XOR,NOT,WIRE}
Gset 6	{AND,OR,XOR,NOT,NAND,NOR,WIRE}

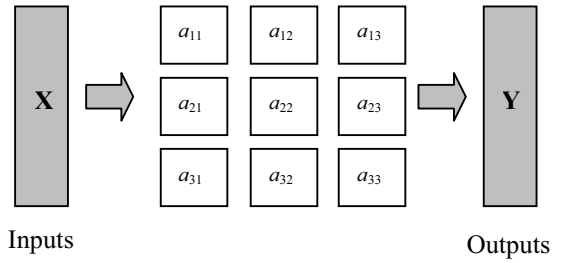

Fig. 40. A 3 × 3 matrix representing a circuit with input *X* and output *Y*.

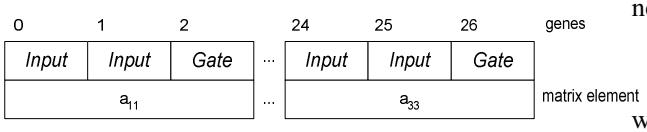

Fig. 41. Chromosome for the 3 × 3 matrix of Fig. 40.

The basic concept of the PSO technique lies in accelerating each particle towards its *pbest* and *gbest* locations with a random weighted acceleration. However, in our case we also use a kind of mutation operator that introduces a new cell in 10% of the population. This mutation operator changes the characteristics of a given cell in the matrix. Therefore, the mutation modifies the gate type and the two inputs, meaning that a completely new cell can appear in the chromosome.

To run the PSO we have also to define the number *P* of individuals to create the initial population of particles. This population is always the same size across the generations, until reaching the solution.

The calculation of the fitness function F_s in (41) has two parts, f_1 and f_2, where f_1 measures the functionality and f_2 measures the simplicity. In a first phase, we compare the output *Y* produced by the PSO-generated circuit with the required values Y_R, according with the truth table, on a bit-per-bit basis. By other words, f_1 is incremented by one for each correct bit of the output until f_1 reaches the maximum value f_{10}, that occurs when we have a functional circuit. Once the circuit is functional, in a second phase, the algorithm tries to generate circuits with the least number of gates. This means that the resulting circuit must have as much genes <*gate type*> ≡ <*wire*> as possible. Therefore, the index f_2, that measures the simplicity (the number of null operations), is increased by *one* (*zero*) for each *wire* (*gate*) of the generated circuit, yielding:

$$f_{10} = 2^{ni} \times no \tag{41a}$$

$$f_1 = f_1 + 1 \text{ if } \{\text{bit } i \text{ of } \mathbf{Y}\} = \{\text{bit } i \text{ of } \mathbf{Y_R}\}, \quad i = 1, \ldots, f_{10} \tag{41b}$$

$$f_2 = f_2 + 1 \text{ if } \textit{gate type} = \textit{wire} \tag{41c}$$

$$F_s = \begin{cases} f_1, & F_s < f_{10} \\ f_1 + f_2, & F_s \geq f_{10} \end{cases} \tag{41d}$$

where *ni* and *no* represent the number of inputs and outputs of the circuit.

The concept of dynamic fitness function F_d results from an analogy between control systems and the GA case, where we master the population through the fitness function. The simplest control system is the proportional algorithm; nevertheless, there can be other control algorithms, such as, for example, the proportional and the differential scheme.

In this line of thought, expression (41) is a static fitness function F_s and corresponds to using a simple proportional algorithm. Therefore, to implement a proportional-derivative evolution the fitness function needs a scheme of the type (Reis *et al.*, 2005b):

$$F_d = F_s + KD^{\mu}[F_s] \tag{42}$$

where $0 \leq \mu \leq 1$ is the differential fractional-order and $K \in \Re$ is the 'gain' of the dynamical term.

9.3 Experiments and Results

A reliable execution and analysis of an EC algorithm usually requires a large number of simulations to provide a reasonable assurance that the stochastic effects are properly considered. Therefore, in this study are developed $n = 20$ simulations for each case under analysis.

The experiments consist on running the three algorithms {GA, MA, PSO} to generate a typical combinational logic circuit, namely a 2-to-1 multiplexer (*M2-1*), a 1-bit full adder (*FA1*), a 4-bit parity checker (*PC4*) and a 2-bit multiplier (*MUL2*), using the fitness scheme described in (41) and (42). The circuits are generated with the gate sets presented in Table 6 and $P = 3000$, $w = 0.5$, $c_1 = 1.5$ and $c_2 = 2$.

Figure 42 depict the standard deviation of the number of generations to achieve the solution *S(N) versus* the average number of generations to achieve the solution *Av(N)* for the algorithms {GA, MA, PSO}, the circuits {*M2-1*, *FA1*, *PC4*, *MUL2*} and the gate sets {2, 3, 4, 6}. In these figure, we can see that the *MUL2* circuit is the most complex one, while the *PC4* and the *M2-1* are the simplest circuits. It is also possible to conclude that *Gset 6* is the less efficient gate set for all algorithms and circuits.

Figure 42 reveals that the plots follow a power law:

$$S(N) = a[Av(N)]^b \quad a, b \in \Re \tag{43}$$

Table 7 presents the numerical values of the parameters (*a*, *b*) for the three algorithms.

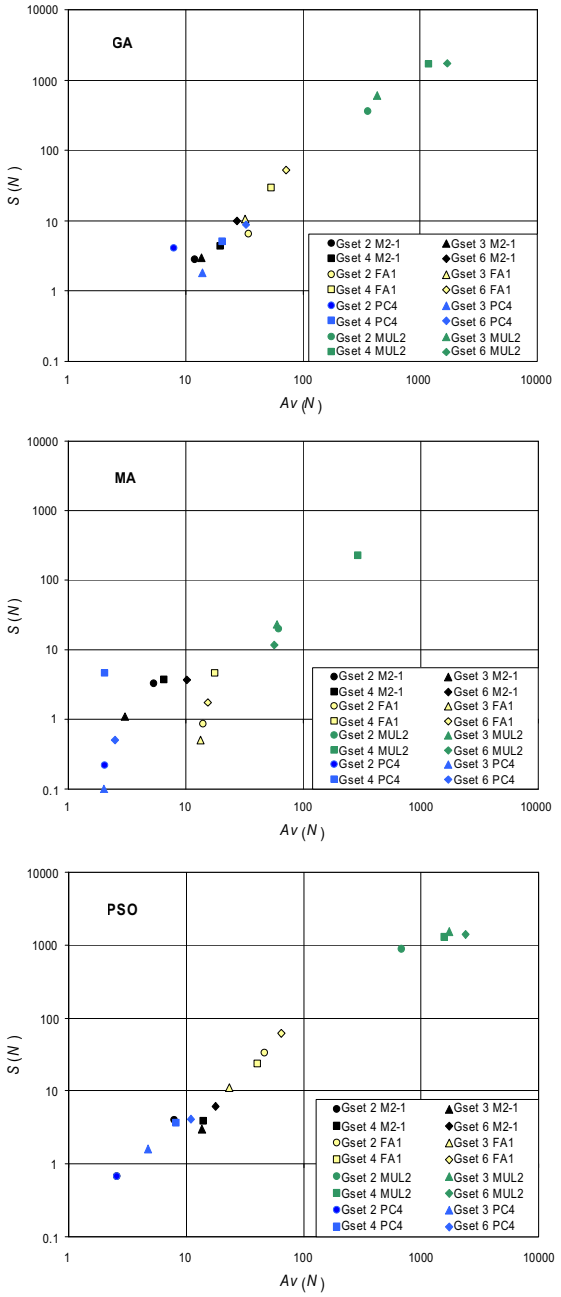

Fig. 42. $S(N)$ *versus* $Av(N)$ with P = 3000 and F_s for the GA, the MA and the PSO algorithms.

Table 7. The Parameters (a, b) and (c, d)

Algorithm	a	b	c	d
GA	0.0365	1.602	0.1526	1.1734
MA	0.0728	1.2602	0.2089	1.3587
PSO	0.2677	1.1528	0.0141	1.1233

In terms of $S(N)$ *versus* $Av(N)$, the MA algorithm presents the best results for all circuits and gate sets. In what concerns the other two algorithms, the PSO is superior (inferior) to the GA for complex (simple) circuits.

Figure 43 depict the average processing time to obtain the solution $Av(PT)$ *versus* the average number of generations to achieve the solution $Av(N)$ for the algorithms {GA, MA, PSO}, the circuits {*M2-1, FA1, PC4, MUL2*} and the gate sets {2, 3, 4, 6}. When analysing these charts it is clear that the PSO algorithm demonstrates to be around ten times faster than the MA and the GA algorithms.

These plots follow also a power law:

$$Av(PT) = c\left[Av(N)\right]^{d} \quad c,d \in \Re \tag{44}$$

Table 7 shows parameters (c, d) and we can see that the PSO algorithm has the best values.

Figures 44 and 45 depict the standard deviation of the number of generations to achieve the solution $S(N)$ and the average processing time to obtain the solution $Av(PT)$, respectively, *versus* the average number of generations to achieve the solution $Av(N)$ for the PSO algorithm using F_d, the circuits {*M2-1, FA1, PC4, MUL2*} and the gate sets {2, 3, 4, 6}. We conclude that F_d leads to better results in particular for the *MUL2* circuit and for the $Av(PT)$.

Figures 46 and 47 present a comparison between F_s and F_d.

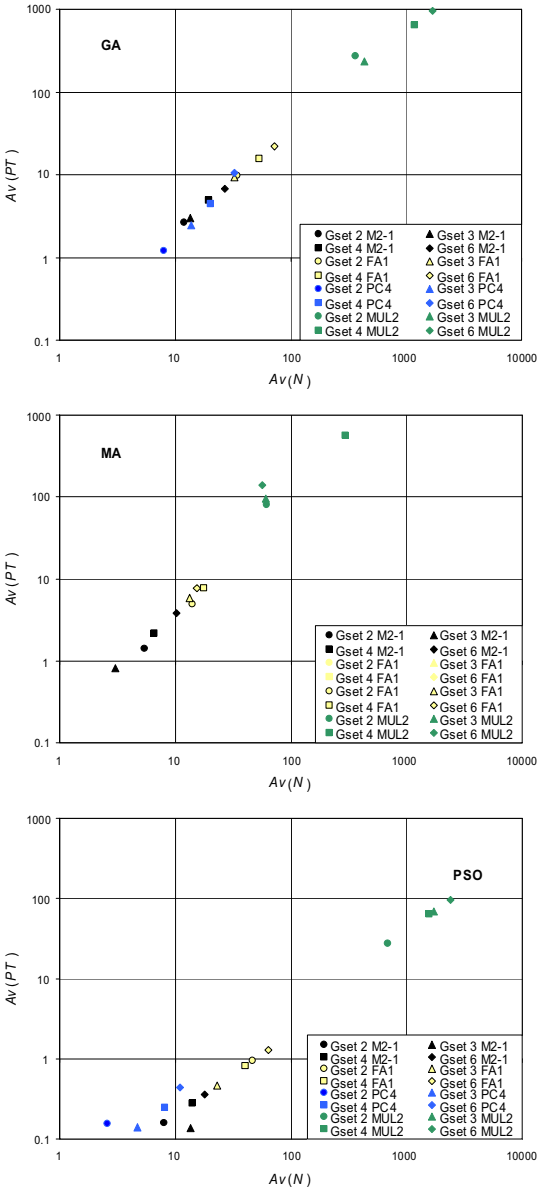

Fig. 43. $Av(PT)$ *versus* $Av(N)$ with P = 3000 and F_s for the GA, the MA and the PSO algorithms.

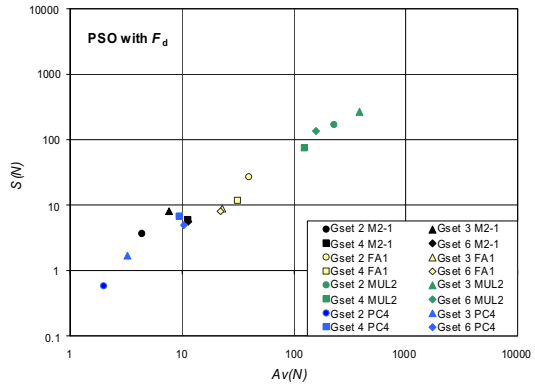

Fig. 44. *S*(*N*) *versus Av*(*N*) for the PSO algorithm, $P = 3000$ and F_d .

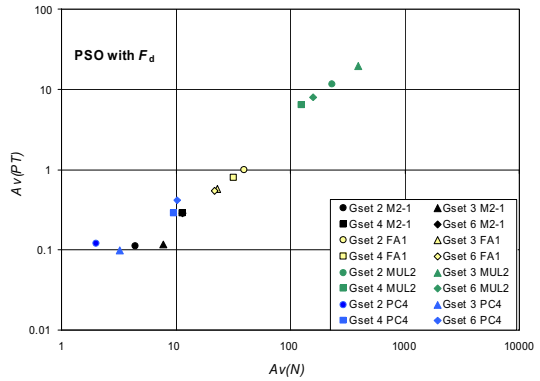

Fig. 45. *Av*(*PT*) *versus Av*(*N*) for the GA, $P = 3000$ and F_d.

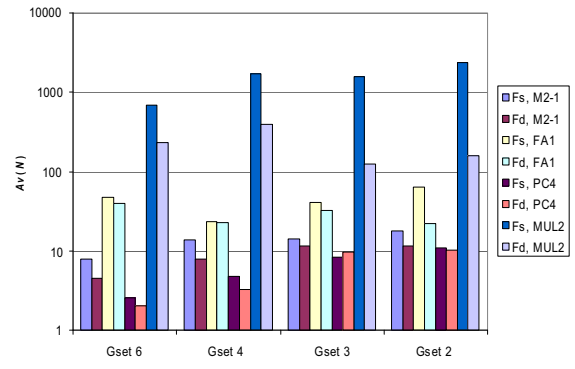

Fig. 46. *Av*(*N*) for the PSO algorithm, $P = 3000$ using F_s and F_d.

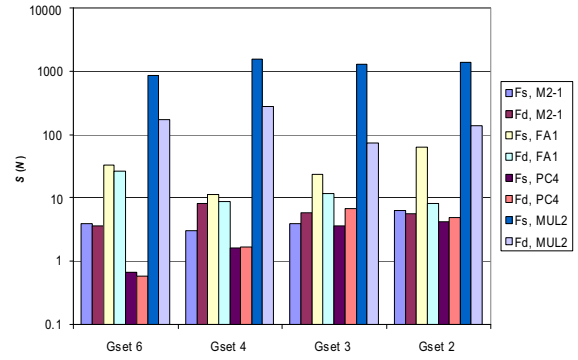

Fig. 47. *S*(*N*) for the PSO algorithm, $P = 3000$ using F_s and F_d.

In terms of *S*(*N*) *versus Av*(*N*) it is possible to say that the MA algorithm presents the best results. Nevertheless, when analysing Fig. 43, that shows *Av*(*PT*) *versus Av*(*N*) for reaching the solutions, we verify that the PSO algorithm is very efficient, in particular for the more complex circuits.

The PSO based algorithm for the design of combinational circuits follows the same profile as the other two evolutionary techniques presented in this paper.

Adopting the study of the *S(N) versus Av(N)* for the three evolutionary algorithms, the MA algorithm presents better results over the GA and the PSO algorithms. However, in what concerns the processing time to achieve the solutions the PSO outcomes clearly the GA and the MA algorithms. Moreover, applying the F_d the results obtained are improved further in all gate sets and in particular for the more complex circuits.

10. DYNAMICS IN A PARTICLE SWARM OPTIMIZATION ALGORITHM

This section studies the fractional dynamics during the evolution of a Particle Swarm Optimization (PSO) algorithm. Some swarm initial particles are randomly changed for stimulating the system response, and its effect is compared with a reference situation. The perturbation effect in the PSO evolution is observed in the perspective of the time behavior of the fitness of the best particle. The dynamics is investigated through the median of a sample of experiments, while adopting the Fourier analysis for describing the phenomena. The influence of the PSO parameters upon the global dynamics is also observed by performing several experiments for distinct values and parameters.

10.1 PSO Algorithm

The particle swarm optimization algorithm was proposed originally by Kennedy and Eberhart (1995). This optimization technique is inspired in the way swarms (*e.g.*, flocks of birds, schools of fishes, herds) elements move in a synchronized way as a defensive tactic. An analogy is established between a particle and an element of swarm. The particle movement is characterized by two vectors representing its current position x and velocity v (Fig. 48).

Initialize Swarm
repeat
  forall particles *do*
    Calculate fitness *f*
  end
  forall particles *do*
    $v_{t+1} = I\, v_t + \phi_1(b\text{-}x) + \phi_2(g\text{-}x)$
    $x_{t+1} = x_t + v_{t+1}$
  end
until stopping criteria

Fig. 48. Particle Swarm Optimization.

10.2 The Optimization System

This section presents the problem used in the study of the *optimization* PSO dynamic system. The objective function consists on minimizing the Easom function (45) (Bergh and Engelbrecht, 2006). This function has two parameter and the optimum function is located at $f(x_1,x_2)|_{opt}$=-1.0. The variables consist in $x_1, x_2 \in [-100,100]$ and the algorithm uses real code to represent the swarm.

$$f(x_1,x_2) = -\cos(x_1)\cos(x_2)\,\mathrm{e}^{-(x_1-\pi)^2-(x_2-\pi)^2} \quad (45)$$

A 50-population PSO is executed during 5000 generations under $\phi_1 = \phi_2 = 1.5$.

The influence of several factors can be analyzed in order to study the dynamics of the PSO (Pires *et al*., 2006), particularly the inertia factor I or the ϕ_i constants, $i = \{1, 2\}$. This effect can vary according to the type of population size, fitness function, and generation number used in the PSO. In this work, it is changed randomly one particle of the initial population. The influence of the inertia parameter is studied by performing tests for the values $I = \{0.4, 0.5, \ldots, 0.8\}$. The fitness evolution of the best global particle is taken as the output signal.

10.3 The PSO Dynamics

The PSO system is stimulated by perturbing the initial population, namely by replacing one particle by a one new generated randomly. The corresponding swarm population fitness modification Δf is evaluated. The test condition remains unchanged during all the experiments. Therefore, the variation of the resulting PSO swarm fitness perturbation during the evolution can be viewed as the output signal that varies during the successive iterations. This analysis is evaluated using several experiments with different perturbation that replace the same particle in the population. All the other particles remain unchanged.

In this perspective, a perturbation input signal is created in the initial population when the replacement is performed. The output signal consists in the difference between the population fitness with and without the initial perturbation, that is $\Delta f(T) = f_{pert}(T) - \mathrm{f}(T)$.

Once having de Fourier description of the output signals it is possible to calculate the corresponding normalized transfer function (46) for particle replacement n_r.

$$H(\mathrm{j}w) = \frac{F\{\delta f_i(T)\}(\mathrm{j}w)}{F\{\delta p_{m\,i}(T)\}(\mathrm{j}w=0)} \quad (46)$$

After repeating for all seeds a `representative' transfer function is obtained by using the median of the statistical sample (Machado and Galhano, 1998) of n experiments for inertial term of I. In Fig. 49 are depicted the transfer functions for $I = 0.4$ up to $I = 0.8$.

After repeating for all seeds a `representative' transfer function is obtained by using the median of the statistical sample (Machado and Galhano, 1998) of n experiments (see Fig. 49). The medians of the transfer functions calculated previously (*i.e.*, for each real and imaginary part and for each frequency) are taken as the final part of the numerical transfer function $H(\mathrm{j}w)$.

Therefore, the median of the numerical system transfer functions, Fig. 49, is approximated by analytical expressions with gain $k = 1$, one pole $a \in \Re^+$ of fractional order $\alpha \in \Re^+$, and a time delay T, given by (47) (see Fig.50).

$$G_i(\mathrm{j}w) = \frac{k\,\mathrm{e}^{-T}}{\left(\frac{\mathrm{j}w}{a}+1\right)^{\alpha}} \quad (47)$$

For evaluating the influence of the inertia parameter I are performed several simulations ranging from $I = 0.4$ up to $I = 0.8$. The parameters of $\{a, \alpha, T\}$ are depicted in Fig. 51.

The results reveal that the transfer function parameters $\{a, \alpha, T\}$ have some dependence with the inertia coefficient I. It can be observed that the parameters of transfer function have a maximum values at $I = 0.6$.

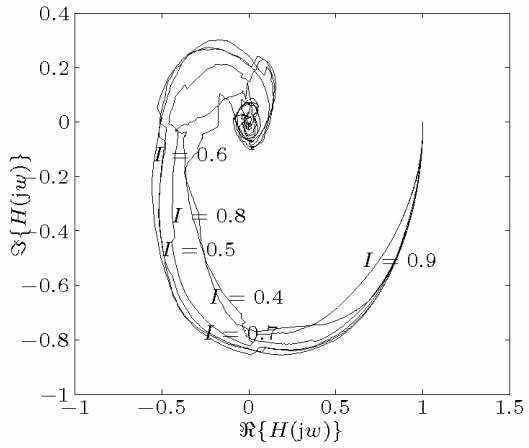

Fig. 49. Median transfer function $H(\mathrm{j}w)$, $n_r = \{4,5,\ldots 8\}$.

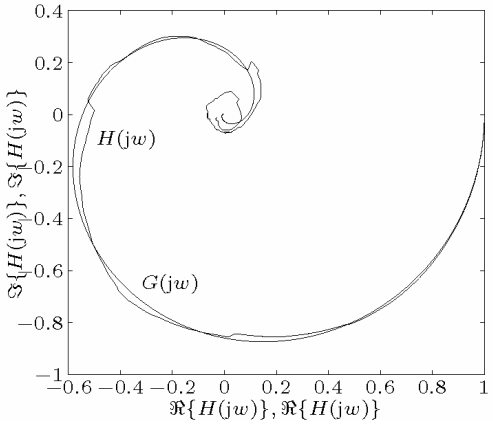

Fig. 50. Polar diagram for $\{H(\mathrm{j}w), G(\mathrm{j}w)\}$, $P = 0.6$.

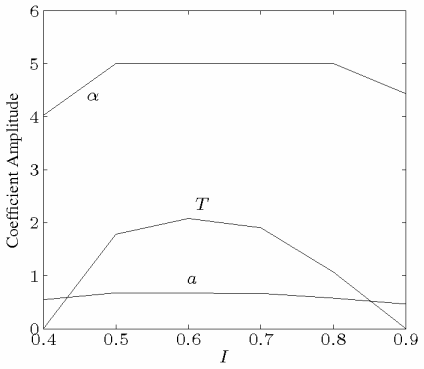

Fig. 51. Parameters (a, α, T) of $G(jw)$.

By enabling the zero/pole order to vary freely, we get non-integer values for α, while the adoption of an integer-order transfer function would lead to a larger number of zero/poles to get the same quality in the analytical fitting to the numerical values. The "requirement" of fractional-order models in opposition with the classical case of integer models is a well-known discussion and even nowadays final conclusions are not clear since it is always possible to approximate a fractional frequency response through an integer one as long as we make use of a larger number of zeros and poles. Nevertheless, in the present experiments there is a complementary point of view towards FC.

This section analyzed the signal propagation and the dynamic phenomena involved in the time evolution of a swarm. The study was established on the basis of the Easom function optimization. While PSO schemes have been extensively studied, the influence of perturbation signals over the operating conditions is not well known.

11. CONCLUSIONS

We have presented several applications of the FC concepts. It was demonstrated the advantages of using the FC theory in different areas of science and engineering. The results demonstrate the importance of Fractional Calculus in the modeling and control of many systems and motivate for the development of new applications.

REFERENCES

Barbosa, R. S., J. A. T. Machado and I. M. Ferreira (2004a). Tuning of PID Controllers Based On Bode's Ideal Transfer Function. *Nonlinear Dynamics* **38**(1-4), 305-321.

Barbosa, R. S., J. A. T. Machado, I. M. Ferreira and J. K. Tar (2004b). Dynamics of the Fractional – Order Van der Pol Oscillator. In: *Proceedings of the IEEE International Conference on Computational Cybernetics*, Vienna, Austria.

Barsoukov, E. and J. R. Macdonald (2005). *Impedance Spectroscopy, Theory, Experiment, and Applications*. John Wiley & Sons.

Bay, J. (1992). Geometry and Prediction of Drift-free trajectories for Redundant Machines Under Pseudoinverse Control, *International Journal of Robotics Research* **11**, 41-52.

Bergh, F. V. and A. P. Engelbrecht (2006). A Study of Particle Swarm Optimization Particle Trajectories. *Inf. Sci.* **176**(8), 937-971.

Charef, A., H. H. Sun, Y. Y. Tsao and B. Onaral (1992). Fractal System Represented by Singularity Function. *IEEE Transactions on automatic Control* **37**(9), 1465-1470.

Chiaverini, S. (1997). Singularity-Robust Task-Priority Redundancy Resolution for Real Time Kinematic Control of Robot Manipulators. *IEEE Trans. Robotics Automation* **13**, 398-410.

Chung, W. J., Y. Youm and W. K. Chung (1994). Inverse Kinematics of Planar Redundant Manipulators via Virtual Links with Configuration Index. *J. of Robotic Systems* **11**, 117-128.

Conkur, E. S. and R. Buckingham (1997). Clarifying the Definition of Redundancy as Used in Robotics. *Robotica* **15**, 583-586.

Doty, K. L., C. Melchiorri and C. Bonivento (1993). A Theory of Generalized Inverses Applied to Robotics. *International Journal of Robotics Research* **12**, 1-19.

Duarte, F. and J. A. T. Machado (2002). Chaotic Phenomena and Fractional-Order Dynamics in the Trajectory Control of Redundant Manipulators. *Nonlinear Dynamics* **29**(1-4), 315-342.

Falconer, K. (2003). *Fractal Geometry Mathematical Foundation and Applications*. John Wiley & Sons.

Feeny, B. F. (2004). Fractional Derivatives Applied to Phase Space Reconstruction. *Nonlinear Dynamics* **38**(1-2).

Goldberg, D. E. (1989). *Genetic Algorithms in Search Optimization and Machine Learning*. Addison-Wesley.

Hilfer, R. (2000). *Applications of Fractional Calculus in Physics*. World Scientific, Singapore.

Hirad S., Ali Hajimiri, Arvin R. Shahani, Gitty N. Nasserbakht and Thomas H. Lee (1998). Fractal Capacitors. *IEEE Journal of Solid-State Circuits* **33**(2), 2035-2041.

Jesus, I. S., J. A. Tenreiro Machado, J. Boaventura Cunha and Manuel F. Silva (2006a). Fractional Order Electrical Impedance of Fruits and Vegetables. In: *Proceedings of the 25th IASTED International Conference on Modeling, Identification and Control - MIC 2006*, Spain.

Jesus, I. S., J. A. T. Machado and J. B. Cunha (2006b). Application of Genetic Algorithms to the Implementation of Fractional Electromagnetic Potentials. In: *Proceedings of the Fifth International Conference on Engineering Computational Technology - ECT 2006*, Civil-Comp Press, Las Palmas de Gran Canaria, Spain.

Jonscher, A. K. (1993). *Dielectric Relaxation in Solids*. Chelsea Dielectric Press, London.

Kennedy, J. and R. C. Eberhart (1995). Particle Swarm Optimization. In: *Proceedings of the*

IEEE International Conference Neural Networks, pp. 1942-1948.

Klein, C.A and C. C Huang (1983). Review of Pseudoinverse Control for Use With Kinematically Redundant Manipulators. *IEEE Trans. Syst. Man, Cyber.* **13**, 245-250.

Liebovitch, L. S. (1998). *Fractals and Chaos Simplified for the Life Sciences*. Oxford University Press.

Lima, M. F. M, J. A. Tenreiro Machado and Manuel Crisóstomo (2005). Experimental Set-Up for Vibration and Impact Analysis in Robotics. *WSEAS Trans. on Systems* **5**(4), 569-576.

Lima, M. F., J. A. T. Machado and M. Crisóstomo (2006). Fractional Order Fourier Spectra In: Robotic Manipulators With Vibrations. *Second IFAC Workshop on Fractional Differentiation and its Applications*. Porto, Portugal.

Louis, S. J., Rawlins and G. J. Designer (1991). Genetic Algorithms: Genetic Algorithms in Structure Design. In: *Proceedings. of the Fourth Int. Conference on Genetic Algorithms*.

Machado, J. T. (1997). Analysis and Design of Fractional-Order Digital Control Systems. *SAMS -Journal Systems Analysis-Modelling-Simulation* **27**, 107-122.

Machado, J. A. T. and A. M. Galhano (1998). A Statistical Perspective to the Fourier Analysis of Mechanical Manipulators. *Journal Systems Analysis-Modelling-Simulation* **33**, 373-384.

Machado, J. A. T. (2001). Discrete-Time Fractional-Order Controllers. *FCAA Journal of Fractional Calculus & Applied Analysis* **4** (1), 47–66.

Marcos, M. G., F. B. M. Duarte and J. A. T. Machado (2007). Complex Dynamics in the Trajectory Control of Redundant Manipulators. *Nonlinear Science and Complexity*, 134-143.

Miller, K. S. and B. Ross (1993). *An Introduction to the Fractional Calculus and Fractional Differential Equations*. Wiley & Sons, NY.

Nakamura, Y. (1991). *Advanced Robotics: Redundancy and Optimization*. Addinson-Wesley.

Oldham, K. B. and J. Spanier (1974). *The Fractional Calculus*. Academic Press, NY.

Oustaloup, A. (1991). *La Commande CRONE: Commande Robuste d'Ordre Non Entier*. Editions Hermès, Paris.

Oustaloup, A. (1995). *La Dérivation Non Entière.* Editions Hermès, Paris.

Oustaloup, A., X. Moreau and M. Nouillant (1997). From fractal robustness to non integer approach in vibration insulation: the CRONE suspension. In: *Proceedings of the 36th Conference on Decision & Control*. California, USA.

Peters, E. E. (1996). *Chaos and Order in Capital Market: A new view of cycles, prices and market volatility*. Wiley Finance Editions, NY.

Pires, E. J., J. A. T. Machado and P. B. de Moura Oliveira (2006). Dynamical Modelling of a Genetic Algorithm. *Signal Processing* **86**(10), 2760-2770.

Podlubny, I. (1999). *Fractional Differential Equations*. Academic Press, San Diego.

Ramirez, J. A., M. Cisneros, C. Ibarra-Valdez and A. Soriano (2002). Multifractal Hurst analysis of crude oil prices. *Physica A* **313**(3), 651-670.

Reis, C., J. A. T. Machado and J. B. Cunha (2005a). An Evolutionary Hybrid Approach in the Design of Combinational Digital Circuits. *WSEAS Transactions on Systems* **4**, 2338-2345.

Reis, C., J. Machado and J. Cunha (2005b). Evolutionary Design of Combinational Circuits Using Fractional-Order Fitness. In: *Proceedings of the Fith EUROMECH Nonlinear Dynamics Conference*, pp. 1312–1321.

Roberts, R. R. and A. Maciejewski (1994). Singularities, Stable Surfaces and Repeatable Behavior of Kinematically Redundant manipulators. *International Journal of Robotics Research* **13**, 70-81.

Samko, S. G., A. A. Kilbas and O. I. Marichev (1993). *Fractional Integrals and Derivatives: Theory and Applications*. Gordon and Breach Science, Amsterdam.

Seereeram, S. and J. T. Wen (1995). A Global Approach to Path Planning for Redundant Manipulators. *IEEE Trans. Robotics Automation* **11**, 152-159.

Shi, Y. and R. C. Eberhart (1998). A Modified Particle Swarm Optimizer. In: *Proceedings of the 1998 International Conf. on Evolutionary Computation*, pp. 69-73.

Siciliano, B. (1990). Kinematic Control of Redundant Robot Manipulators: A Tutorial. *Journal of Intelligent and Robotic Systems* **3**, 201-212.

Silva, M. F., J. A. T. Machado, and A. M. Lopes (2003a). Comparison of Fractional and Integer Order Control of an Hexapod Robot. In: *Proceedings of the VIB 2003 – ASME Int. 19th Biennial Conf. on Mech. Vib. and Noise*, USA.

Silva, M. F., J. A. T. Machado and A. M. Lopes (2003b). Position / Force Control of a Walking Robot. *MIROC – Machine Intelligence and Robot Control* **5**, 33 – 44.

Silva, M. F., J. A. T. Machado and A. M. Lopes (2005). Modelling and Simulation of Artificial Locomotion Systems. *Robotica* **23**, Issue 5, 595 – 606.

Silva, M. F., J. A. T. Machado and R. S. Barbosa (2006a). Complex-Order Dynamics in Hexapod Locomotion. *Signal Processing* **86**, Issue 10, 2785 – 2793.

Silva, M. F. and J. A. T. Machado (2006b). Fractional Order PD^{α} Joint Control of Legged Robots. *Journal of Vibration and Control* **12**(12), 1483 – 1501.

Szu, H. P. (1984). *Applied Fourier Analysis*.University of Evansville, Harcourt Brace Jovanovitch, Publishers, NY.

Trendafilova, L. and H. Brussel (2001). Nonlinear Dynamics tools for the motion Analysis and condition monitoring of Robot Joints. *J. Mech. Systems and Signal Processing* **15(**6), 141-1164.

Yoshikawa, T. (1988). *Foundations of Robotics: Analysis and Control*. MIT Press.